Spring 2023

Using Capillary Electrophoresis to Quantify Competitive Binding of Adsorbates to Silver Nanoparticles

Christopher D. Chung , '23

Using Capillary Electrophoresis to Quantify Competitive Binding of Adsorbates to Silver Nanoparticles

Presented as a Senior Course Thesis in Chemistry

Christopher Chung
May 15th, 2023
Swarthmore College
Advisor: Kathryn Riley

Table of Contents

List of Common Abbreviations

AgNPs – silver nanoparticles
BSA – bovine serum albumin
CE – capillary electrophoresis
CD – circular dichroism spectroscopy
DLS – dynamic light scattering
EM – electron microscopy
ENM – engineered nanomaterial
ICP-MS – inductively-coupled plasma mass spectroscopy
K_a – association constant
K_d – dissociation constant
k_{on} – rate constant of association
k_{off} – rate constant of dissociation
NECEEM – Nonequilibrium capillary electrophoresis for equilibrium mixtures
NOM – natural organic matter
PC – protein corona
PDI – polydispersity index
SEM – scanning electron microscopy
SRHA – Suwannee River humic acid
TEM – transmission electron microscopy
UV-vis – ultraviolet visible spectroscopy

List of Figures

Abstract

Silver nanoparticles (AgNPs) are increasingly used commercially and medically due to their antimicrobial and antibacterial properties. With increased use comes increased release of AgNPs into the environment, and once released, AgNPs can form coronas with molecules ranging from biomolecules to proteins to natural organic matter (NOM). The molecules in the corona adsorb to the surface of the AgNPs, drastically altering their innate properties such as cytotoxicity and binding behavior. In this study, we characterize and quantify model AgNP-adsorbate systems by obtaining their relevant reaction parameters through three different affordable analytical techniques, including dynamic light scattering (DLS), UV-vis spectroscopy, and capillary electrophoresis (CE). Citrate-stabilized AgNPs with hydrodynamic diameters of 10 nm, 20 nm and 40 nm were used in this work. K_a values of AgNPs reacting with a model protein, bovine serum albumin (BSA) and a model NOM, Suwannee River humic acid (SRHA), were individually quantified using UV-vis spectroscopy. Nonequilibrium capillary electrophoresis of equilibrium mixtures (NECEEM) was also employed to obtain binding and rate constants pertaining to the individual reactions and compared with the values acquired through UV-vis spectroscopy. The AgNP size was shown to have an indirect relationship with their reactivity, with smaller AgNPs having higher K_a values. There was also remarkable agreement between the two quantitative analyses, validating the use of the novel NECEEM technique for use in other NP corona complexes. DLS was used to characterize the initial nanoparticles as well as those with a formed corona, and circular dichroism (CD) spectroscopy was used to monitor protein conformational changes upon adsorption of BSA to AgNPs and interaction with SRHA. Subsequently, in a field dominated by single adsorbate studies of the AgNP coronas, we strived to take this study a step further and investigate multiple adsorbate systems. Thus, a new CE-based pull-down assay was developed and optimized for quantitative analysis of the relative reactivity of multiple adsorbates interacting with AgNPs. Using this new technique, SRHA was found to decrease the amount of BSA adsorbed to AgNPs in solution across all sizes. Smaller sized AgNPs seemed to favor BSA adsorption over SRHA, but as the size of the AgNP increased, the affinity seemed to shift to favoring the adsorption of SRHA.

Chapter I: Introduction

1.1 Overview of silver nanoparticles

Engineered nanomaterials (ENMs) are widely used in the modern-day world due to their unique properties. In particular, silver nanoparticles (AgNPs) are increasingly used in commercial and medical applications. About 320 tons of AgNPs are produced each year due to their strong antimicrobial and antifungal properties.[1] Commercially, AgNPs are found in a wide variety of products, including textiles such as sportswear to target odor-causing bacteria and medical clothing, including masks, gowns, and gloves, to prevent the spread of harmful bacteria. Medically, AgNPs have paved way for a multitude of possibilities in treating various diseases. For example, once they enter the human body, NPs can slip past the detection of phagocytes and evade the immune system.[2–4] This allows for targeted drug delivery in the human body using the AgNPs as carriers. AgNPs also have presented themselves as a possible means of cancer treatment. Studies have shown that AgNPs introduced into the human body may induce apoptosis of malevolent cancer cells.[5]

With the abundant production of AgNP-enhanced products, concern over their environmental fate has risen. In 2010, it was estimated that 63-91% of over 260,000 – 309,000 metric tons of the global ENMs produced ended up in landfills.[6] In the specific case of AgNPs, up to 105 μg/L total silver concentration was detected in the liquid influx of wastewater treatment plants.[7] It is not surprising that so much silver is released into the environment since AgNPs readily dissolve and can be easily released from commercial products.[8–16] A study by Benn et al. showed that AgNPs could be easily released from commercial socks by simply immersing them in water with agitation.[17] While sludge

from wastewater treatment facilities is a prominent destination for AgNPs released into the environment, AgNPs can also end up in a multitude of other environmental compartments such as air, soil and eventually, in the human body.[8]

In the human body, ENMs, while praised for their versatility in commercial and medical goods, have been shown to have toxic effects.[18] Some types of NPs were discovered to have carcinogenic properties,[19] cause lung inflammation,[20] and promote cardiovascular misfunctions, albeit *in vivo*.[21] Specifically looking at AgNPs, an average human intakes around 0.4 to 30 μg of silver from their environment, namely through the air inhaled and the food and water ingested.[22] AgNPs, especially smaller ones with a hydrodynamic diameter of 10 nm or less, have been shown to malevolently affect normal human cell lines in the liver, respiratory system, digestive tract, urinary tract, cardiovascular system, nervous system, the reproductive system and even the sensory organs.[23] The cytotoxic properties of AgNPs have been shown to depend not only on their size, but also on the AgNP concentration, pH of the medium, and exposure to pathogens.[24] While the current human exposure levels to AgNPs are low and haven't shown significantly malignant effects to human health,[23] it is important to note that the increased use and improper disposal of AgNPs will lead to increased human exposure and potentially to increased toxicity. What's more, the environmental impact of AgNPs has yet to be fully understood and could include toxic effects to specific organisms as well significant alterations to microbial communities.[25–28]

Whether unintentionally released into the environment or intentionally used in medical applications, AgNPs are rarely found in their pristine (as synthesized) form. Instead, AgNPs form "coronas," or shells of material that are adsorbed onto the AgNP

surface.[29] This tendency is primarily attributed to the increase in entropy with the adsorption of materials onto the AgNP surface and the nonspecific interactions between the materials and the highly energized AgNP surface.[30] The identity of the adsorbed material and the composition of the corona depends on the environment in which the AgNPs are found. The most prominent of the adsorbed material that will be studied in this work are proteins and natural organic matter (NOM). The formation of AgNP coronas can drastically alter AgNP behavior, including their physicochemical characteristics, functionality, biodistribution and cytotoxicity.[31] While the toxicity of pristine AgNPs is well studied and known, the role of AgNP coronas to mediate toxicity is poorly understood,[32,33] which is concerning based on the surge of ENM development and its commercial use in the recent years.

1.2 Protein and Eco-coronas

Generally, the interaction of AgNPs with proteins is governed by the following equilibrium:

$$n\ Protein + AgNP \rightleftharpoons Protein_n - AgNP \quad (1)$$

Layers of proteins adsorb onto the AgNP surface through protein-AgNP and protein-protein interactions to form the protein corona (PC).[29] The PC formed at the early stages of the reaction is often dominated by the most abundant proteins, where the first proteins that reach the AgNP surface adsorb immediately. However, as the reaction equilibrates, more and more proteins adsorb to the AgNPs and eventually, more suitable protein molecules with higher binding affinities replace the original ones on the NP surface, forming what is called a hard corona. This displacement of low affinity proteins with

high affinity proteins is called the Vroman effect. [2,34] Once the hard corona is formed, protein-protein interactions can lead to the formation of additional PC layers, called the soft corona.[35] Soft coronas are dynamic and frequently changing due to constant protein adsorption/desorption, while hard coronas are usually more temporally stable. The soft corona can change its identity when it encounters different compartments within the environment, or even in the human body, making it harder to study *in vivo*.[4,25,35–40]

Proteins are not the only adsorbates that can form AgNP coronas.[32] For example, environmental molecules like NOM, inorganic ions, organic pollutants, and other biomolecules (e.g., lipids, DNA, etc) can form what is called an eco-corona.[41] Since AgNPs are ubiquitously found in aquatic media such as waste water, they come in contact with a variety of NOM and biomolecules excreted from organisms inhabiting the area.[42,43] Thus, the environment in which the AgNPs inhabit strongly influences the composition of the eco-coronas formed.[32] Eco-coronas have just as much capacity to cause the change in fate of AgNPs released into the environment, including organismal uptake and trophic transfer.[13,32,44–46] Although eco-coronas are not nearly as extensively studied as PCs, recent studies illustrate the importance of eco-corona formation on the environmental impact of ENMs.[41–43] The formation of eco-coronas have actually been shown, with a few exceptions, to reduce ENM toxicity to organisms in the environment by affecting the ENMs' adsorption, stabilization, dissolution, and surface chemistry.[42,43] Research specifically related to AgNP eco-coronas is still quite limited, which this work aims to address.

Ultimately, the formation of AgNP coronas, whether protein or eco-coronas, imparts a new biological identity and reactivity on the AgNPs, which alters their fate,

transport, and toxicity.[47] It has been shown that preexisting protein corona structures can alter the ability of further proteins to adsorb to AgNP surfaces. Some proteins in the complex can act as binding sites for other free-floating proteins in solution, having a recruiting effect. Others can nonspecifically adsorb to the AgNP surface and block binding sites, having an inhibiting effect for other proteins' adsorption.[3,35] These observed properties have inspired scientists to manipulate AgNP surfaces to create patient-specific corona structures for applications in medical settings,[3] but also has implications for potential toxicity mechanisms of AgNPs. While the previous consensus on AgNP toxicity to cells was that it was largely dependent on dissolution, recent studies have shown that AgNPs themselves can have toxic effects on cells through particle specific pathways.[5,13,25,39,48–51] As aforementioned, AgNPs with protein coronas can elude cell defensive mechanisms and become internalized in cells. There, they can alter cell homeostasis through alteration of protein behavior or through particle-specific interactions with organelles inside the cell.[3,5,52] The question still remains of what toxic effects eco-coronas can impart on cells, making studying the eco-corona imperative.

1.3 Methods for Quantifying Corona Formation

When studying eco-coronas, it is essential to characterize the particles and the corona to fully understand specific mechanisms for toxicity. Thus, the following section will largely introduce contemporary methods to quantify corona formation, including those used in this work and those proposed for future studies.

1.3.1 Electron Microscopy

Previous work pertaining to ENMs has used a variety of techniques to characterize and study their nanoscale properties. One such method, is electron microscopy (EM), which allows for better resolution in images of samples produced compared to traditional optical microscopes. It uses accelerated electron beams as a source to visualize nanomaterials.[53] Various types of EMs have been developed to perform different tasks, including scanning EM (SEM), transmission EM (TEM), volume EM (vEM) and cryo-EM. The most widely used of these types are SEM and TEM. EM uses a series of metal apertures and magnetic lenses to focus and accelerate an electron beam onto a sample, where interactions between the electrons and the sample generate signals that give information about the material's surface topography, composition, and other electrical characteristics that can be transformed into an image.[53] SEM mainly uses the reflection of the electrons off of the surface of the material in order to characterize surface morphology of the samples and can achieve up to 500,000× magnification.[54] TEM, on the other hand, uses the transmission of electrons through the material to create an image of higher quality. In TEM, parameters pertaining to the structure of material such as lattice type, chemical composition, crystallographic details, phase-type, and morphological details can be obtained.[54,55] In high-resolution mode, TEM allows for up to 1,000,000× magnification of the sample.[53]

Specific to this work, TEM can be used to visualize the formation of coronas around AgNPs. For example, TEM has been used to image AgNP interactions with molecules such as cellulose nanofibers and different reducing ligands.[56,57] Other studies have visualized the interaction of AgNPs with proteins like bovine serum albumin (BSA)

and NOMs like humic acid.[30,58] While TEM can provide visual evidence of corona formation, quantitative parameters regarding the strength of the interactions cannot be obtained.

1.3.2 Circular Dichroism Spectroscopy

Circular dichroism (CD) spectroscopy is an analytical technique that takes advantage of circularly polarized light being absorbed differently for chiral molecules depending on their handedness.[59] Circularly polarized light is focused onto the sample solution, and the spectrometer measures the difference in absorbance by the chiral molecules pertaining to right and left (clockwise and counterclockwise) circularly polarized light. Various modes of CD analysis can be specified for different molecules, one of which is vibrational CD. Vibrational CD can be used to probe structures of chiral molecules.[60–62] However, more traditionally, absorption in the UV region has been used to rapidly characterize protein secondary structure due to the characteristic peaks observed for α-helix and β-pleated sheet secondary structures.[59,63–65] Absorbance differences at characteristic wavelengths can be used to quantify of the degree of secondary structure changes in sample solutions. Specific to this work, it was found that the peak at 208 nm in the CD spectrum correlates well with quantifying α-helical structures.[66–68] In this work, CD will be used to probe differences in protein secondary structure caused by introduction of AgNPs into solution and the subsequent corona complex formation mechanisms.

1.3.3 Dynamic Light Scattering

The formation of protein or eco-coronas typically leads to a change in the hydrodynamic diameter and surface charge of AgNPs. Dynamic light scattering (DLS) is ideally suited to provide qualitative confirmation of corona formation since it measures the hydrodynamic diameter and zeta potential of particles in a liquid medium (Figure 1).[69] DLS uses a monochromatic laser to probe the Brownian motion of particles in solution.[70] Light from the laser is scattered by particles onto a detector, creating a unique scattering pattern. As particles move in solution, the detected scattering pattern is shifted in the *x*-*y* plane and becomes uncorrelated from the original signal. The rate at which the scattering pattern becomes uncorrelated can be related to the particle size using a mathematical correlation function, with smaller particles undergoing more rapid change and larger particles undergoing slower change (Figure 1**A**).[69]

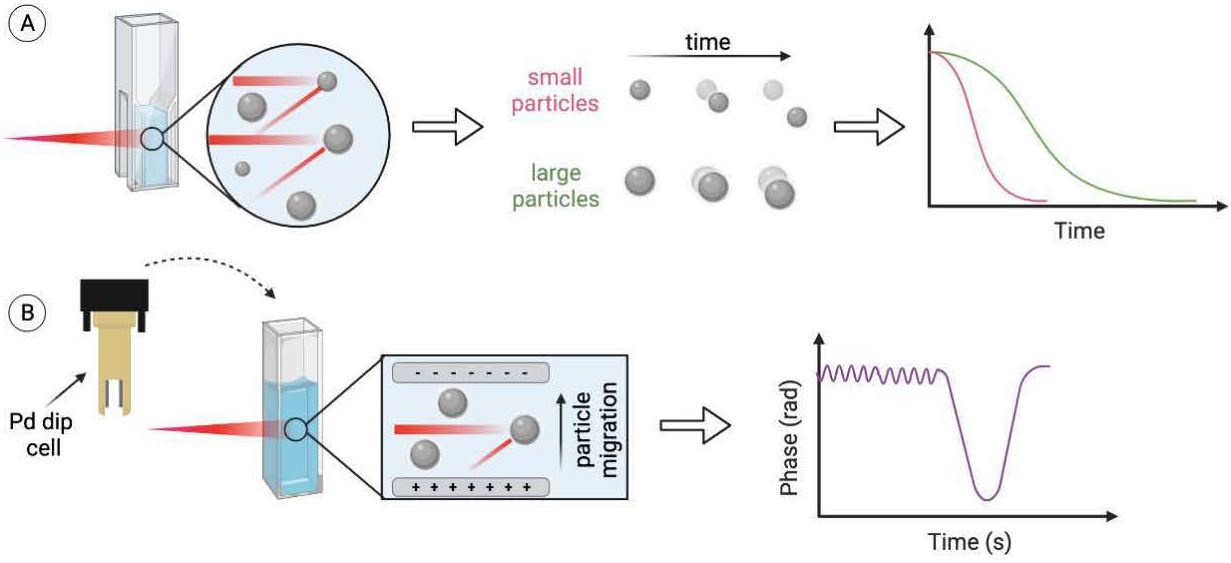

Figure 1. Schematic of DLS analysis for determation of the **(A)** hydrodynamic diameter and **(B)** zeta potential of AgNPs.

DLS can also be used to measure the zeta potential of particles in solution. In this case, a Pd dip cell is inserted into the cuvette containing the colloidal solution, and an electric field is formed between the two electrodes of the dip cell (Figure 1**B**). As was the case with measuring the hydrodynamic diameter of the particles, a monochromatic laser is focused through the sample and used to probe the velocity at which the particles move under the applied electric field. This is accomplished by measuring the phase shift of the scattered beam, which is proportional to the particle velocity. Then, the phase shift is used to determine the electrophoretic mobility of the particles, from which the zeta potential can be calculated using the Henry equation (Figure 1**B**).

1.3.4 UV-vis Spectroscopy

Plasmonic nanoparticles, like AgNPs, have unique optical properties based on parameters such as their size and shape. They also exhibit localized surface plasmon resonance (LSPR) effects.[71–74] LSPR describes the collective oscillation of electrons on the surface of the AgNPs at a frequency that is resonant with the frequency of the incident electromagnetic radiation. For AgNPs, this collective oscillation gives rise to characteristic LSPR absorption bands in the visible region of the electromagnetic spectrum, making UV-vis spectroscopy a useful tool to probe AgNPs. The LSPR band is largely dependent on NP characteristics that include their size, charge, and surface chemistry, all of which can be observed in a UV-vis spectrum.

Beyond qualitative observations about AgNP properties, UV-vis can be used as a quantitative analysis method by analyzing changes in the LSPR band of the spectrum. With the adsorption of corona constituents onto the AgNP surface, the LSPR band shifts

towards a longer wavelength because the surface chemistry of the AgNP is transformed. The red shift that occurs here is due to the change of the refractive index of AgNP surfaces caused by the adsorption of molecules.[75] The magnitude of the LSPR shift can be used to calculate the association constant of the AgNP-adsorbate equilibrium (Figure 2).[76] In this study, the wavelength at which the maximum absorbance occurred for each sample was used in order to deduce the association constants using the Langmuir adsorption isotherm model:[76]

$$\frac{\Delta\lambda}{\Delta\lambda_{max}} = \frac{K_a[ads]}{1+K_a[ads]} \quad (2)$$

In this equation, $\Delta\lambda$ is the shift in wavelength of the LSPR band for an AgNP-adsorbate mixture relative to the initial wavelength of the LSPR band (no adsorbate condition); $\Delta\lambda_{max}$ is the maximum shift in the LSPR band; K_a is the association constant for formation of the AgNP-adsorbate complex; and [ads] is the concentration of adsorbate in the particular sample.

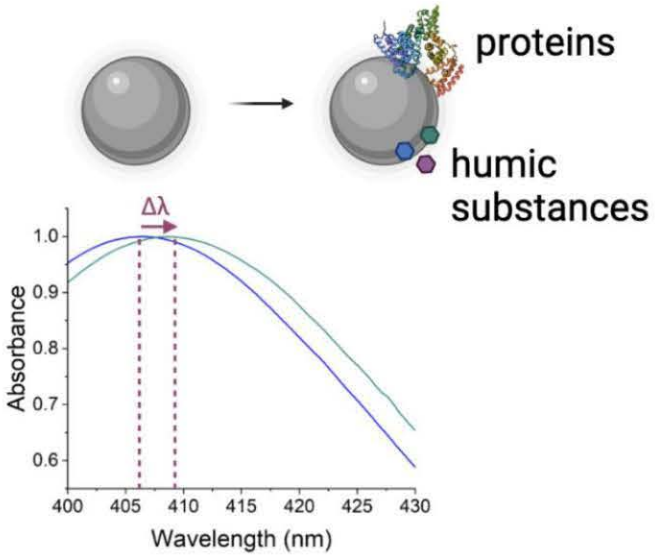

Figure 2. Schematic of the LSPR band of bare AgNPs (blue trace), which shifts to a longer wavelength upon formation of a AgNP eco-corona (green trace).[76]

1.3.5 Capillary Electrophoresis

Capillary electrophoresis (CE) is a separation technique that uses the principles of electroosmotic flow to separate analytes based on charge and size. It uses a basic instrumental set-up where two ends of fused-silica capillary tubing are connected to a high voltage power supply. The capillary is filled with a buffered electrolyte; the sample is injected at the inlet end of the capillary, and the capillary ends are immersed into buffer solutions. Then, an electric field is applied to establish electroosmotic flow in the direction of the outlet end of the capillary and analytes in the sample are separated based on their unique electrophoretic mobilities (Figure 3**A, 3C**).[77–79] An absorbance detector positioned near the outlet end of the capillary is used to detect analytes as they migrate through the capillary (Figure 3**B**).

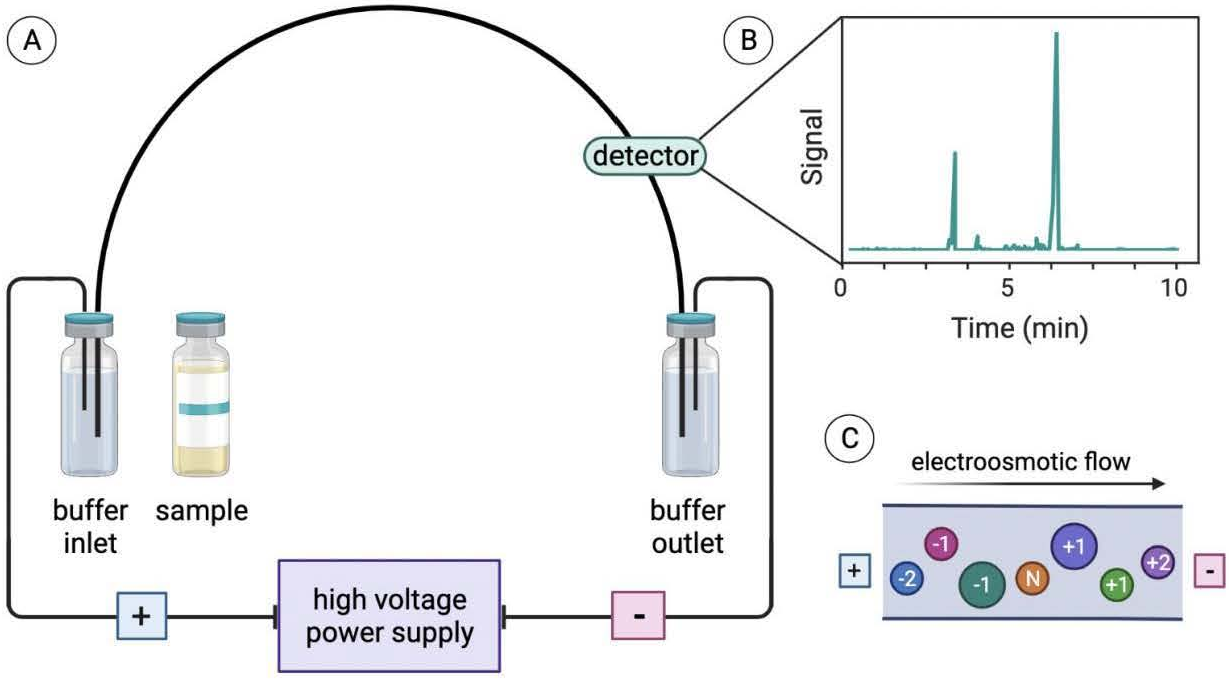

Figure 3. Schematic of capillary electrophoresis. **(A)** Instrument diagram of the CE system. The sample is injected into the capillary and **(B)** analytes are detected using an absorbance detector. **(C)** Analytes are separated according to their size and charge.

Generally, CE is the analytical technique of choice to separate DNA fragments, proteins, small molecules, and ions.[77,80,81] In addition, more advanced CE-based techniques can be used to probe reaction parameters. One such technique, nonequilibrium capillary electrophoresis of equilibrium mixtures (NECEEM), is used in this work to to determine the equilibrium dissociation constant (K_d) and kinetics (k_{on} and k_{off}) for AgNP-adsorbate complexes.[82] Since eco-coronas are in dynamic equilibrium states, the adsorbates are constantly dissociating and reassociating with the AgNPs, which enables their analysis by NECEEM. NECEEM involves the initial injection of an equilibrium mixture containing free AgNPs, free adsorbate, and AgNP-adsorbate complexes into the capillary (**Figure 4A**, t_0). When the voltage is applied and electroosmotic flow is established, each component of the equilibrium mixture begins migrating according to its own electrophoretic mobility, such that as AgNP-adsorbate complexes dissociate, the AgNP and adsorbate begin migrating away from one another in the capillary and cannot reassociate (**Figure 4A**, t_1). This dissociation process causes a shoulder on the AgNP peak in the CE graph (**Figure 4B**, region A_3), which can be used to calculate the dissociation constant, K_d, according to:[83]

$$R = \frac{A_1}{A_2 + A_3} \tag{3}$$

$$K_d = \frac{[Ads]_0(1+R) - [AgNP]_0}{1 + {}^{1}/_{R}} \tag{4}$$

In equation 3, A_1, A_2 and A_3 are the integrated peak areas of unbound AgNPs, region of dissociation and AgNP-P complexes, respectively. In equation 4, $[Ads]_0$ is the initial concentration of adsorbate added, $[AgNP]_0$ is the concentration of the AgNP added and R is the constant derived from equation 3.

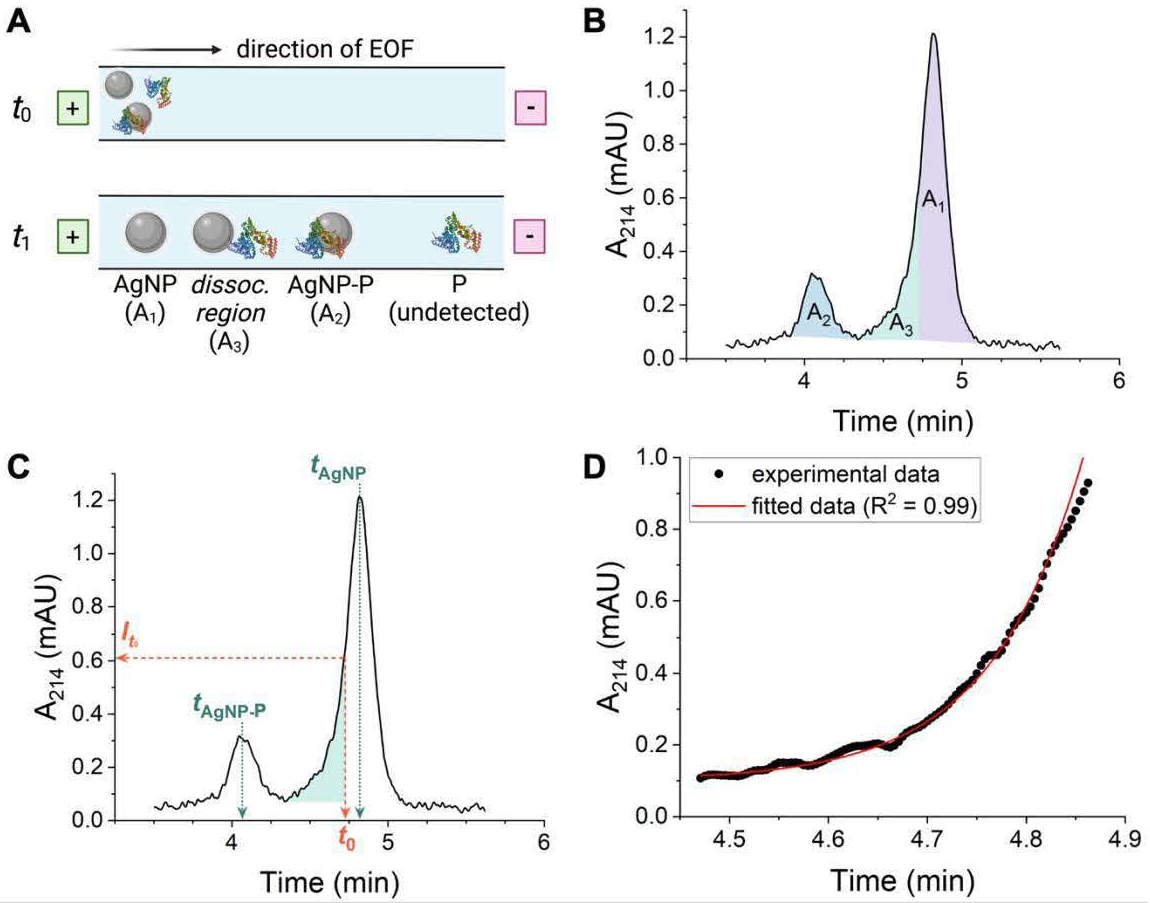

Figure 4. Schematic of the NECEEM assay. **(A)** An equilibrium mixture of AgNPs, a protein (P), and AgNP-P complexes is injected into the capillary (t_0) and each component is separated based on its electrophoretic mobility (t_0). AgNP-P complexes dissociate in the capillary under nonequilibrium conditions, **(B)** which is observed in the CE electropherogram as region A_3. **(C)** Key parameters related to the dissociation region (A_3) can be used to **(D)** fit the electropherogram and obtain kinetics constants.

NECEEM can also be used to calculate the rate constants for the association (k_{on}) and dissociation (k_{off}) reactions. By fitting equation 3 to the electropherogram in the region of dissociation (**Figure 4C-D**), we can calculate the k_{off} value, which can then be used as shown in equation 3 to obtain the k_{on} value.

$$I_t = I_{t_0} e^{\left(k_{off}\left(\frac{t_{AgNP-P}}{t_{AgNP}-t_{AgNP-P}}\right)(t-t_0)\right)} \quad (5)$$

$$k_{on} = {}^{k_{off}}/_{K_d} \quad (6)$$

In equation 3, I_t is the absorbance value at any point in time (y-axis value), I_{t_0} is the absorbance intensity at the right end of the region of dissociation, t_{AgNP-P} is the migration time of the AgNP-protein complex peak (A_2 region in **Figure 4B**), t_{AgNP} is the migration time of the AgNP peak (A_1 region in **Figure 4B**), t is the migration time at any point in time (x-axis value), and t_0 is the time at which the region of dissociation ends. The attainment of all these parameters in a single CE experimental run makes NECEEM a powerful tool for studying monomolecular binding processes between AgNPs and adsorbates.[82]

1.4 Research Aims

With the increased use of AgNPs worldwide and their entrance into environmental soil and water compartments, the formation of AgNP eco-coronas and their effect on the environmental fate, transport, toxicity, and persistence of AgNPs should be studied with relative urgency. Thus, the present work emphasized the development of rapid and affordable analytical techniques to effectively study the interactions between AgNPs and eco-corona constituents in greater depth and with greater quantitative precision. Compared to more traditional techniques like SEM or TEM, the novel CE techniques developed in this work have several benefits, including affordability (as much as 10× reduced cost), the ability to quantify parameters regarding the formation of AgNP eco-coronas (K_d, k_{on}, k_{off}), and fast sample analysis times (less than one hr). These benefits make the CE-based techniques more accessible to the scientific community for similar or new applications.

In this study, we first demonstrate the application of two CE techniques – one based on NECEEM and one based on a pull-down assay – to evaluate AgNP coronas formed from single adsorbates. The model adsorbates include a model protein, BSA, and a model NOM, Suwanee River humic acid (SRHA). All analyses were applied to citrate-stabilized AgNPs of three different diameters (10 nm, 20 nm, and 40 nm) to separately investigate the effect of size on corona formation. K_a values for the reactions of each AgNP size with each adsorbate were obtained through NECEEM and were corroborated using values acquired by a pre-established UV-vis spectroscopy technique based on the Langmuir adsorption isotherm model. AgNP-adsorbate complexes were also qualitatively characterized using DLS and CD spectroscopy.

Next, we expanded beyond the analysis of single-adsorbate systems that are widely used in the literature,[84] to understand how individual binding parameters direct formation of coronas formed from multiple adsorbates (i.e., BSA *and* SRHA). These studies included two binding models – one where corona constituents were allowed to sequentially react with the AgNPs and one where they were introduced simultaneously. Specifically, in sequential binding studies, AgNP-adsorbate complexes were pre-formed with one of the model adsorbates before the addition of the other adsorbate. This model was used to evaluate the effects of a pre-existing corona on the subsequent adsorption of a different adsorbate. In competitive binding studies, both adsorbates were added to the AgNP-containing solution simultaneously and were allowed to "compete" for vacancy on the AgNP surface. Each of these adsorption models was studied using the CE pull-down assay to quantitatively compare relative binding affinities. Again, DLS and CD spectroscopy were used qualitatively to confirm the formation of the complex coronas.

Chapter II: Materials and Methods

2.1 Reagents and Sample Preparation

2.1.1 Reagents Used

Nitric acid solution (70%), sodium bicarbonate (99.5%), Trizma base (99.9%), sodium phosphate dibasic (99%) and BSA were purchased from Sigma-Aldrich (St. Louis, MO). HEPES sodium salt (99%) was purchased from Acros Organics (Geel, Belgium). SRHA (Type III) was purchased from the International Humic Substances Society (Denver, CO) and used as received. Citrate-capped AgNPs of different hydrodynamic diameters 10, 20 and 40 nm and a concentration of 20 mg L^{-1} were purchased from nanoComposix (San Diego, CA) and used as received. All sample preparation steps and measurements were carried out in the dark to eliminate the possibility of photo-induced dissolution or aggregation of the AgNPs.[32]

All analyses were carried out in 10 mM sodium bicarbonate (pH 7.0) buffer, and the solution pH was adjusted through dropwise addition of 1.0 M and 0.1 M HCl. A stock solution of 5 μM BSA was prepared in water and frozen at -20°C in 1 mL aliquots. Frozen BSA stocks were thawed on the day of use and sonicated for 10 minutes to ensure no aggregation of BSA using a Branson M1800H Ultrasonic Cleaner purchased from SonicsOnline (Richmond, VA). A stock solution of 500 mg L^{-1} SRHA was prepared weekly in sodium bicarbonate buffer and sonicated for at least 10 minutes before each use to ensure a homogenous mixture of SRHA in solution.

2.1.2 Pre-concentration of AgNPs

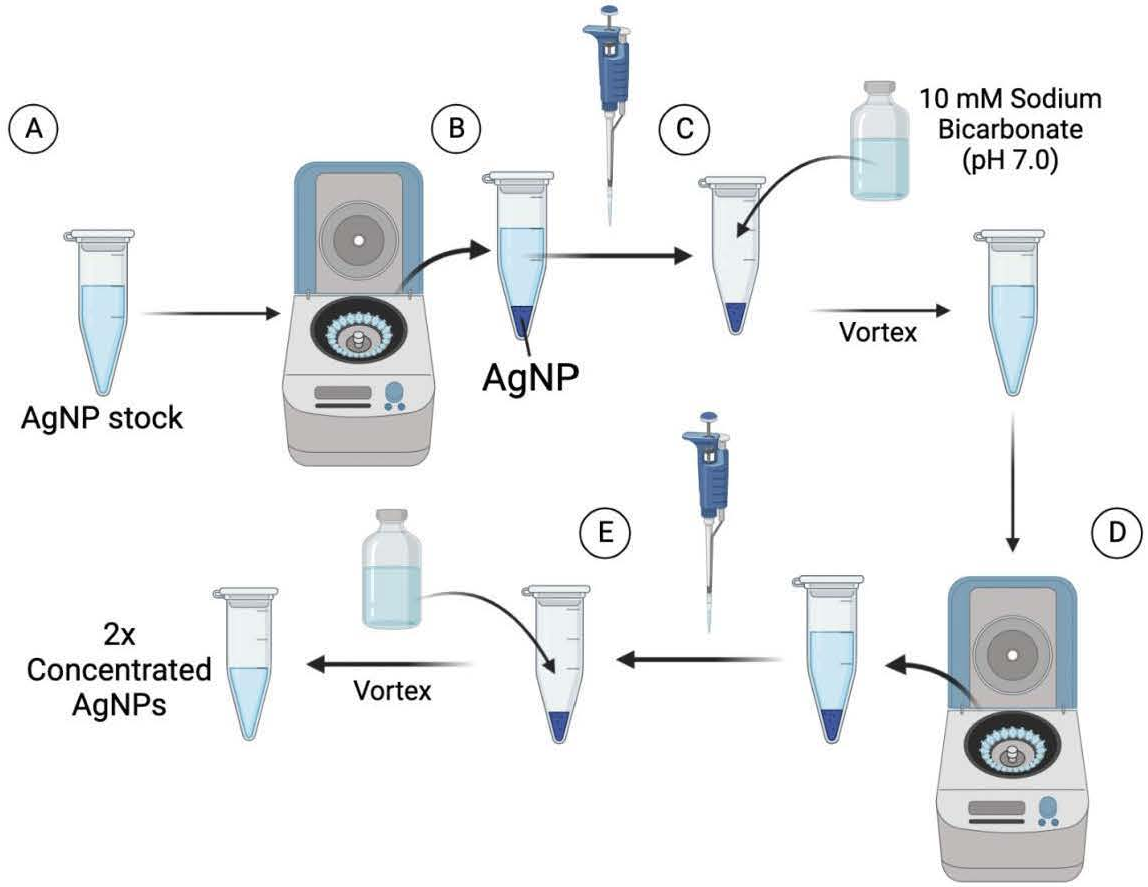

Figure 5. Schematic of the pre-concentration of AgNPs. **(A)** 1 mL AgNP stock solution is centrifuged at 3,900*g* and **(B)** 960 µL of the supernatant is carefully removed. **(C)** 960 µL of the buffer (10 mM sodium bicarbonate pH 7.0) is pipetted back into the Eppendorf tube with the AgNP pellet and vortexed for at least 5 seconds before **(D)** it is centrifuged again at 3,900*g* and 960 µL of the supernatant is removed. **(E)** 460 µL of the buffer is pipetted into the sample to create a 500 µL pre-concentrated solution of AgNPs (2× of the original concentration).

AgNPs of all sizes were pre-concentrated using the protocol outlined in **Figure 5** for the CE, DLS, and CD analyses to obtain sufficient detection sensitivity. An Eppendorf Minispin 5452 Centrifuge was used for centrifugation and a centrifugal force of 3,900*g* was applied for 8 min for 40 nm AgNPs, 15 min for 20 nm AgNPs, and 35 min for 10 nm AgNPs. Successful centrifugation was identified by the colorless appearance of the supernatant, since AgNPs of the sizes studied have a bright yellow color. Following

pre-concentration, the theoretical concentration of all AgNPs was 40 mg L^{-1}. Pre-concentrated AgNPs were prepared before each day of analysis and disposed of the same day, since the highly concentrated AgNP solution was more susceptible to aggregation, even when stored at 4°C.

2.1.3 Sample Preparation of Complexes with Adsorbate

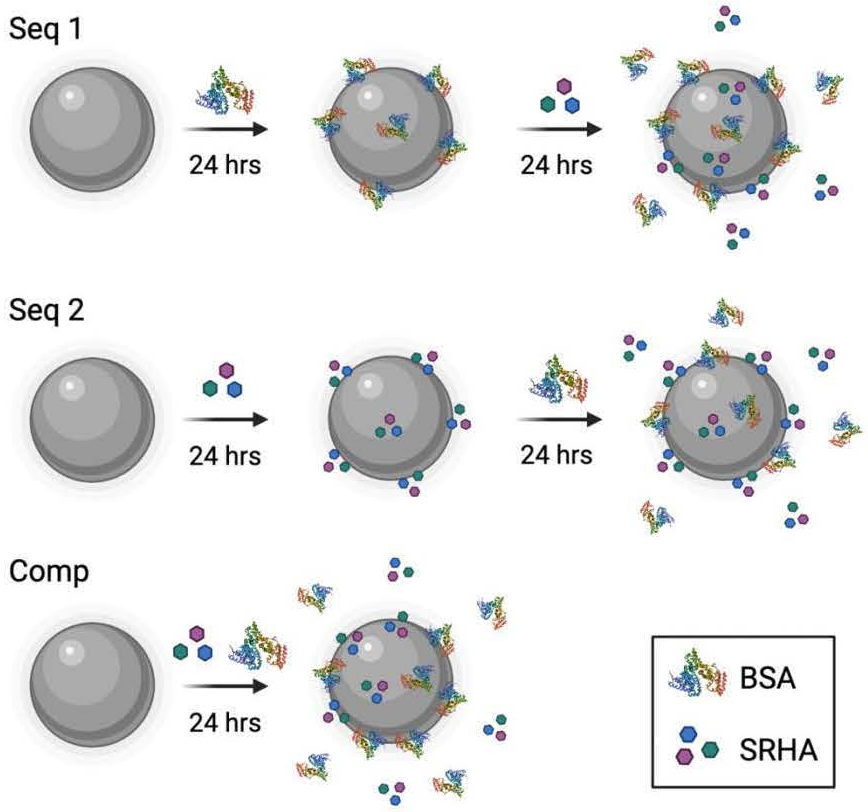

Figure 6. Representation of multiple-adsorbate binding models. Sequential binding models where AgNPs are **(A)** incubated with BSA for 24 hrs followed by 24 hr incubation with SRHA (seq 1) or **(B)** incubated with SRHA for 24 hrs followed by 24 hr incubation with BSA (seq 2). **(C)** Competitive binding model where AgNPs are incubated for 24hrs with a mixture of SRHA and BSA (comp).

Preparation of multi adsorbate systems was done in three different ways – two sequential additions of either adsorbate and one competitive addition (**Figure 6**). For sequential addition 1 (herein, seq1), 1 µM BSA was added into a pre-concentrated AgNP solution, incubated for 24 hrs, and then 60 mg L^{-1} SRHA was added into the mixture and

incubated for an additional 24 hrs. For sequential addition 2 (herein, seq2), 60 mg L^{-1} SRHA was added to a pre-concentrated AgNP solution, incubated for 24 hrs, and then 1 μM BSA was added into the mixture and incubated for an additional 24 hrs. Competitive additions of adsorbates (herein, comp) involved adding 60 mg L^{-1} SRHA and 1 μM BSA simultaneously to a solution of pre-concentrated AgNPs and incubating for 24 hrs prior to analysis. All mixtures were incubated at room temperature in the dark.

2.2 Qualitative Analyses of AgNP and Corona Compositions

2.2.1 Dynamic Light Scattering

The average hydrodynamic diameter (*d.* nm) and zeta potential of AgNPs were measured using a Malvern Zetasizer Nano-ZS Dynamic Light Scattering instrument (Malvern, PA). For DLS measurements, sodium bicarbonate buffer was double-filtered using a 0.2 μm nylon syringe filter. Control samples that contained only 1 μM BSA and only 60 mg L^{-1} SRHA were prepared in triplicate. Samples containing AgNPs only, AgNPs mixed with each individual adsorbate (1 μM BSA or 60 mg L^{-1} SRHA), and AgNPs resulting from each multi-adsorbate incubation (seq1, seq2, and comp) were prepared in triplicate. All samples were prepared in disposable polystyrene cuvettes of 1 cm path length. Prior to DLS analysis, samples were allowed to equilibrate for 2 minutes at 25°C, and 5 replicates of each replicate sample were recorded and averaged. All samples were measured using a backscatter angle of 173°, and for zeta potential measurements, a Pd dip cell was inserted into the cuvette and the Smulochowski equation was applied.

2.2.2 Circular Dichroism

Denaturation effects on the BSA secondary structure were investigated using a Jasco J-1500 CD Spectrometer (Jasco Products Company, Oklahoma City, OK). All samples were prepared in 10 mM sodium bicarbonate (pH 7.0) buffer. Control samples were prepared in triplicate and included those that contained 60 mg L^{-1} SRHA only and 40 mg L^{-1} AgNPs only (pre-concentrated AgNPs). The remaining samples included 1 µM BSA, 1 µM BSA incubated with pre-concentrated AgNPs, and mixtures of 1 µM BSA, 60 mg L^{-1} SRHA and pre-concentrated AgNPs resulting from each multi-adsorbate incubation (seq1, seq2, and comp). Samples were prepared in a macro quartz cuvette with a path length of 1 cm and experiment parameters were as reported previously.[85] For each sample, 7 replicate scans were recorded from 200 to 260 nm. Temperature was controlled with a liquid cooling temperature unit at 25°C, and a bandwidth of 2 nm was used. The alpha helicity of the solutions were calculated using the following equations:[86–88]

$$MRE_{208} = \frac{observed\ CD\ signal\ (mdeg)}{C_P n l \times 10} \quad (7)$$

$$\%\ \alpha - helicity = \left[\frac{-MRE_{208} - 4000}{33{,}000 - 4000}\right] \times 100 \quad (8)$$

where C_P is the molar concentration of the protein, n is the number of amino acids in the protein, l is the path length of the cuvette, and MRE_{208} is the mean residue ellipticity of the random coil conformation at 208 nm.

2.3 Quantitative Analyses of AgNP and Corona Compositions

2.3.1 UV-Vis Spectroscopy

UV-Vis spectroscopy measurements were carried out using a Cary 3500 Multicell UV-Vis purchased from Agilent Technologies (Santa Clara, CA). Semi-micro quartz

cuvettes of 1 cm path length were purchased from Hellma Analytics (Plainview, NY). Samples for Langmuir adsorption isotherms involved incubation of 4 mg L^{-1} of AgNPs with increasing concentrations of BSA (0 - 500 nM) or SRHA (0 - 20 mg L^{-1}). Samples were incubated in Eppendorf tubes for 24 hrs at room temperature in the dark. All samples were prepared in triplicate. Prior to analysis, the instrument was allowed to warm up for 30 min, and a reference cuvette containing sodium bicarbonate buffer was utilized. A baseline was obtained for three different cuvettes containing just buffer before sample analysis. Then, the cuvettes were rinsed with a portion of the sample before loading the sample into the cuvette. Cuvette rinsing with the next sample to be analyzed prior to sample loading was continued throughout the analysis to minimize dilution effects. Working from low-to-high adsorbate concentration, the triplicate samples were analyzed in parallel. For 10 and 20 nm AgNPs, absorbance spectra were recorded from 380 to 415 nm. Since the peak of the LSPR band for 40 nm AgNPs was around 410 nm, absorbance spectra were recorded from 390 to 430 nm for the 40 nm AgNPs. For BSA Langmuir adsorption isotherms, a scan rate of 60 nm per minute was used. For SRHA, the scanning rate was halved to 30 nm per minute to obtain better resolution since the AgNP-SRHA complexes did not exhibit as significant of a red shift of the LSPR band as the BSA complexes.

2.3.2 Capillary Electrophoresis

All samples were prepared in low protein binding microcentrifuge tubes purchased from Thermo Fisher Scientific (Waltham, MA) to minimize the non-specific adsorption of adsorbates onto the surfaces of the centrifuge tubes. A Sciex P/ACE MDQ Plus Capillary Electrophoresis system was used to record all measurements, and the

MDQ Plus software was used for instrument control and data analysis. Each sample was prepared in triplicate and each replicate sample was analyzed in triplicate using the CE, totaling nine different electropherogram measurements for each sample preparation condition. The capillary had an inner diameter of 50 μm, a total length of 60.2 cm, and an effective length (from inlet to detector) of 50.0 cm. Each day, the capillary was primed by flushing for 10 min with water, 10 min with 1 M NaOH solution, 10 min with water, and 20 min with 10 mM sodium bicarbonate (pH 7.0) buffer. Samples were injected hydrodynamically for 5.0 sec at 4.0 psi (35 nL injection volume), a 25 kV separation voltage was applied (415 V/cm), and electropherograms were recorded for 11 min. In between each measurement, the capillary was flushed for 1 min of water and 2 min of sodium bicarbonate buffer to ensure all residual sample was removed from the capillary and that it was filled with buffer for the next experiment.

All AgNP stock solutions were pre-concentrated using the pre-concentration technique described previously (see Section 2.1.2). For the NECEEM assay, pre-concentrated AgNPs were mixed with increasing concentrations of BSA (100 nM, 200 nM, and 300 nM for 20 and 40 nm AgNPs, 50 nM, 100 nM and 150 nM for 10 nm AgNPs) or SRHA (10 mg L^{-1}, 15 mg L^{-1}, and 20 mg L^{-1}). All samples were prepared in triplicate, vortexed at least 5 seconds to ensure a homogenous mixture, and incubated for 24 hrs at room temperature in the dark. For the pull-down assay, a mixture solution of the 1 μM BSA and 60 mg L^{-1} SRHA was made prior to sample preparation, and the stock solution was used to prepare samples in AgNP pre-concentrated solutions. Using the stock solution, a calibration curve was prepared on the same day including 5 points ranging from 0.5 μM to 1.5μM BSA and 20 mg L^{-1} to 100 mg L^{-1} SRHA. Calibration

standards were prepared in 10 mM sodium bicarbonate (pH 7.0) buffer. Pull-down assay samples were prepared in triplicate at 250 µL. They included 1.00 µM BSA (BSA only) or a mixture of 1.00 µM and 60 mg L^{-1} SRHA (BSA + SRHA). After 24 hours of incubation, samples were centrifuged at 3,900*g* according to AgNP size, and 160 µL of the supernatant was carefully pipetted out for CE analysis. After each sample run, peak intensities were quantified using the MDQ Plus software, and concentrations of experimental samples were deduced through fitting to the calibration curve. After all runs, samples containing AgNPs had the % bound of the adsorbates normalized with the control sample to account for any nonspecific adsorption.

Chapter III: Analysis of Single Adsorbate AgNP Coronas Formed from BSA or SRHA

Before moving on to more complex multi-adsorbate systems, single adsorbate studies were performed to qualitatively and quantitatively analyze the AgNP coronas formed in solution. Control samples included BSA only, SRHA only, and AgNPs only, while single adsorbate samples refer to AgNPs incubated with either BSA or SRHA to form a homogeneous corona. All AgNP-containing samples were prepared for each AgNP size (10 nm, 20 nm, and 40 nm). Qualitative analyses of single adsorbate coronas included analysis of the hydrodynamic diameter and zeta potential of the samples using DLS. CD measurements were also used to semi-qualitatively probe the effect of AgNPs on BSA secondary structure, since denaturation of the proteins after formation of the corona complex has previously been used as a marker for gauging protein binding behavior.[76] UV-Vis Langmuir isotherms and NECEEM were used as quantitative assays to calculate reaction parameters for the single adsorbate interaction with differently sized AgNPs. Specifically for the UV-Vis Langmuir isotherms, the K_a for both adsorbates, BSA and SRHA, were discerned, while for NECEEM, the K_a, K_d, k_{on} and k_{off} parameters for BSA were calculated.

3.1 Qualitative Evidence of BSA and SRHA Adsorption to AgNPs

Using DLS, two markers can act as evidence of corona formation: an increase in hydrodynamic size and a change in zeta potential. Since DLS measures a hydrodynamic diameter of the AgNPs (as opposed to the core diameter), the layer of adsorbates around

the AgNP due to corona formation leads to subtle increases in hydrodynamic diameter. Similarly, depending on the charge of the adsorbates forming the corona, changes in the AgNP zeta potential may be observed.

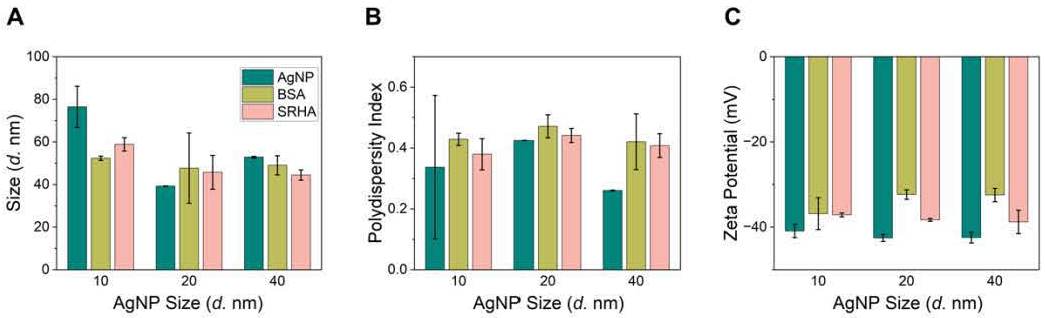

Figure 7. DLS measurements of 10, 20, and 40 nm AgNPs and their single adsorbate coronas formed from BSA or SRHA. **(A)** Hydrodynamic size **(B)** PDI and **(C)** zeta potential of pre-concentrated AgNPs (AgNP), 1 μM BSA with pre-concentrated AgNPs (BSA) and 60 mg L^{-1} SRHA with pre-concentrated AgNPs (HA) in solution.

Changes in the hydrodynamic diameter of the AgNPs upon formation of the BSA or SRHA corona were measured. First, analyzing the AgNPs alone, slight aggregation was observed for all particle sizes (**Figure 7A**; see also **Figure A1**, **Table A1**). The pre-concentration step, which involved centrifugation of the AgNPs, may have resulted in a small degree of aggregation. Upon addition of BSA, a decrease in the hydrodynamic diameter of the AgNPs was observed for the 10 nm and 40 nm AgNPs. However, for the 20 nm AgNPs, an increase in hydrodynamic diameter was evident, adhering to the marker of a slight increase indicating corona formation. For the 10 nm and 40 nm AgNPs, the addition of adsorbates seemed to stabilize the AgNPs against aggregation by increasing the distance between individual AgNPs. Finally, upon addition of SRHA, similar trends were observed where for 10 nm and 40 nm AgNPs, a decrease in hydrodynamic size was observed, while for the 20 nm AgNPs, a slight increase in hydrodynamic size was seen. There does not seem to be much distinction between the

differences in AgNP size upon addition of BSA or SRHA, which is encouraging as both systems were hypothesized to only form a monolayer around the AgNPs.

Next the polydispersity index (PDI) was analyzed, which reports on the homogeneity of the sample. A highly monodisperse and homogeneous sample has a PDI closer to 0 and an aggregated and heterogeneous sample has a PDI closer to 1. The large error bar in the PDI of the bare 10 nm AgNPs also supports the proposed aggregation of the sample based on hydrodynamic diameter measurements (**Figure 7B**). With aggregation in the 10 nm AgNPs, the heterogeneity of the sizes of the individual particles increased, leading to large fluctuations in PDI between different replicates of the same sample. Upon addition of BSA or SRHA, there is an increase in PDI across all three AgNP sizes consistent with an aggregated solution of AgNPs and in contrast to the apparent stabilizing effect of the adsorbates based on decreases in hydrodynamic diameter. Due to these disparities, zeta potential measurements were used as a primary marker for corona formation in single adsorbate systems.

Unlike the size measurements, zeta potential measurements showed a more consistent charge for the stock solutions of all three AgNP sizes, so it was deemed a more reliable marker in analyzing corona formation. For all the zeta potential samples across the three AgNP sizes, the charge shielding effect was evident (**Figure 7C**). Zeta potential values increased (became less negative) with the addition of either adsorbate for the 10, 20, and 40 nm AgNPs. In the case of 20 and 40 nm AgNPs, BSA seemed to cause a more drastic change in the zeta potential than SRHA. The zeta potentials of the individual adsorbates were also measured. The zeta potential of a 1 μM solution of BSA was found to be -21 ± 8 mV and of a 60 mg L^{-1} solution of SRHA was found to be -31 ± 3 mV. The

fact that BSA seemed to shield AgNP charge more effectively than SRHA fits well with the inherent charges that were previously measured for each adsorbate. Overall, DLS size and zeta potential measurements indicated that AgNPs were forming coronas under the experimental conditions.

Then, CD analyses were used to visualize any denaturation of the BSA caused by the adsorption onto AgNP surfaces. First, control samples were analyzed that contained AgNPs alone or SRHA alone. Neither AgNPs nor SRHA displayed a CD signal (**Figure A2**), so there was no interference from the AgNPs in the measurement and SRHA-AgNP complexes could not be measured using this technique. Thus, only samples containing BSA were measured using CD. The secondary structure of BSA was largely unaffected by the addition of AgNPs (**Figure 8**). The differences in magnitudes of the representative 208 nm peak in the CD spectra were insignificant between samples with and without AgNPs, rendering the % α-helicity of the BSA in solution largely unchanged (**Table A4**), which is consistent with previous work.[85] However, the change in % α-helicity induced by AgNPs could be undermined by the fact that the protein concentrations are in heavy excess compared to the AgNP concentrations in the samples.

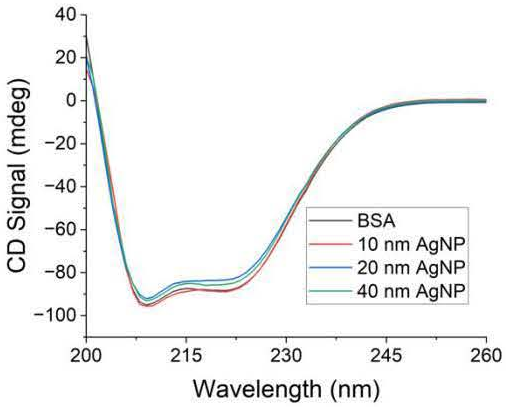

Figure 8. CD spectra of BSA with varying AgNP sizes. The concentration of BSA was 1 μM. AgNPs were pre-concentrated before addition of BSA, and the BSA only sample was prepared in 10 mM sodium bicarbonate (pH 7.0) buffer. All samples were incubated for 24 hrs prior to analysis.

3.2 Quantitative Analysis of AgNP-BSA and AgNP-SRHA Complexes

Table 1. Comparison of UV-vis spectroscopy and NECEEM for measuring AgNP-BSA association constants.

Adsorbate		HA	BSA			
Technique		UV-vis	UV-vis	CE		
Parameter		K_a (L mg^{-1})	K_a (x 10^7 M^{-1})	K_a (x 10^7 M^{-1})	k_{off} (s^{-1})	k_{on} (x 10^6 M^{-1} s^{-1})
d_{AgNP} (nm)	10	0.65 ± 0.06	10.0 ± 0.1	20.7 ± 6	0.017 ± 0.007	3.2 ± 0.6
	20	0.5 ± 0.1	6.4 ± 0.5	11.8 ± 10	0.025 ± 0.007	2.8 ± 2.7
	40	0.48 ± 0.08	7 ± 1	4 ± 1	0.04 ± 0.01	1.7 ± 0.6

Following the qualitative analyses of single adsorbate systems, quantitative assays were performed to discern the K_a values of the reaction between AgNPs and either BSA or SRHA. The novel NECEEM assay was applied to characterize the reaction parameters (K_a, K_d, k_{on} and k_{off}) for both systems. However, due to incomplete separation of AgNP-SRHA complexes from AgNPs in the NECEEM assay, reaction parameters only pertaining to BSA-AgNP complexes were conducted in this study. The concentrations of BSA that were reacted with 20 nm and 40 nm AgNPs were 100, 200 and 300 nM, while lower concentrations of BSA (50, 100 and 150 nM) were needed to obtain characteristic NECEEM electropherograms for the 10 nm AgNPs due to their increased binding affinity. For all conditions, a AgNP peak and a AgNP-adsorbate complex peak were observed from which the equilibrium parameters could be obtained (**Figure A3, Table 1**). The k_{on} values are indirectly correlated with the size of the AgNPs, while the same increase in AgNP size leads to increases in the k_{off} values. This means that with higher k_{on} values, BSA has faster adsorption kinetics with smaller AgNPs, and with lower k_{off}

values, BSA has slower desorption kinetics for smaller AgNPs. This increased affinity for adsorption and decreased affinity for desorption to the AgNP surface led to increasing K_a values for smaller AgNPs (**Table 1, Figure 9**). The increase in reactivity can be attributed to the larger surface area to volume ratio of the smaller AgNPs and changes in surface curvature, which has been observed in other studies. The larger surface area to volume ratio of smaller particles results higher surface energy, which increases the probability of BSA adsorption. Also, surface curvature has been shown to drastically alter binding properties in previous literature.[85,89–91]

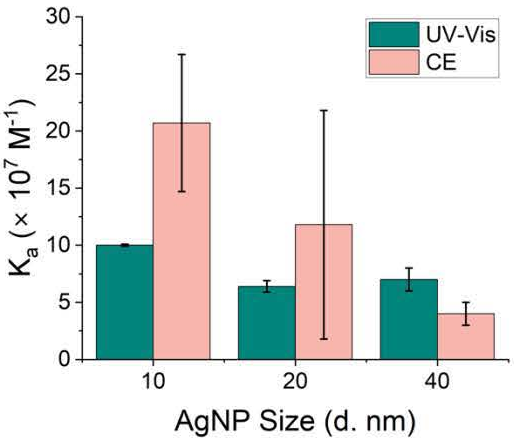

Figure 9. K_a of systems with BSA as adsorbate. K_a values obtained through the UV-Vis Langmuir isotherms and the CE NECEEM assay plotted for 10, 20 and 40 nm AgNPs.

To validate parameters from the NECEEM assay, the K_a values for AgNP-BSA complexes were compared with those obtained using UV-Vis Langmuir adsorption isotherms. Representative Langmuir adsorption isotherm curves are shown for BSA adsorbing to each size of the AgNPs in **Figure 10**. As with the NECEEM assay, the K_a values measured for this procedure held the same trend of smaller AgNPs showing higher reactivity and larger K_a values in the reaction with adsorbates (**Table 1**). There was remarkable agreement between the K_a values obtained through both assays (**Figure 9, Table 1**). Previously, it has been shown that K_a values obtained through other techniques

can range from an order of magnitude of 10^3 to 10^{11} M^{-1}, so the fact that both K_a values obtained through NECEEM and UV-Vis Langmuir isotherms are in the same order of magnitude is promising.[76] This suggests that NECEEM is a reliable assay for probing AgNP-adsorbate complexes with the added benefit that more quantitative parameters (k_{on}, k_{off}) can be obtained compared to the UV-Vis Langmuir isotherm technique.

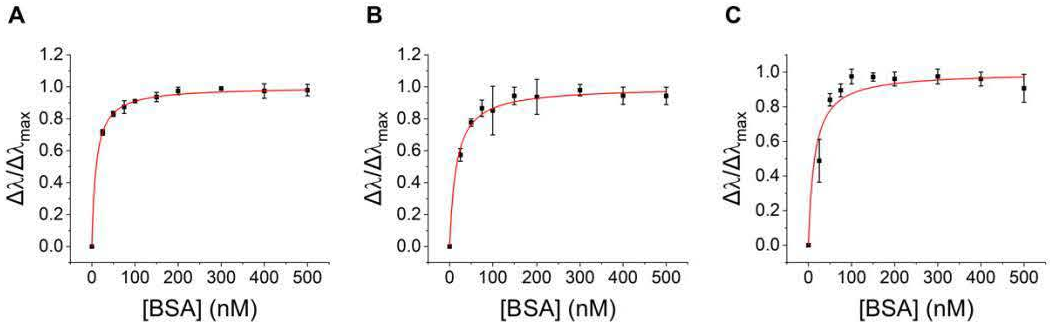

Figure 10. Langmuir adsorption isotherms of AgNP-BSA complexes. Langmuir adsorption isotherms of **(A)** 10 nm AgNPs, **(B)** 20 nm AgNPs, and **(C)** 40 nm AgNPs with concentrations of BSA ranging from 0 to 500 nM. AgNPs were prepared to 4 mg L^{-1} in each sample. All samples were prepared in 10 mM sodium bicarbonate (pH 7.0).

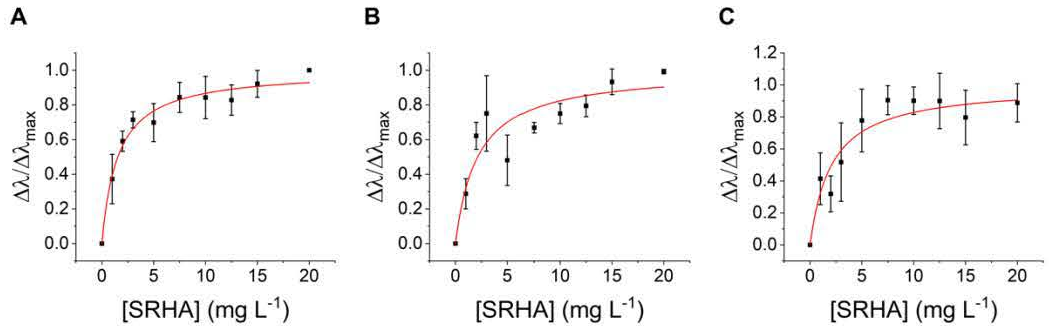

Figure 11. Langmuir adsorption isotherms of AgNP-SRHA complexes. Langmuir adsorption isotherms of **(A)** 10 nm AgNPs, **(B)** 20 nm AgNPs, and **(C)** 40 nm AgNPs with concentrations of SRHA ranging from 0 to 25 mg L^{-1}. AgNPs were prepared to 4 mg L^{-1} in each sample. All samples were prepared in 10 mM sodium bicarbonate (pH 7.0).

The K_a values for SRHA systems were also obtained using the UV-Vis assay (**Figure 11, Table 1**). While the K_a values of SRHA and BSA cannot be used to compare binding affinities to AgNPs due to disparities in the units used to quantify each system, K_a values with SRHA as adsorbate also follow the same trend of decreasing size leading to

increasing reactivities. As was seen in previous literature, in a one-adsorbate system, the AgNP size generally dictates the binding properties with the adsorbate in solution.[85]

Chapter IV: Multi Adsorbate Binding

4.1 Qualitative Evidence of the Formation of a Multi-Adsorbate Corona

Much research has already been performed investigating single adsorbate systems, and like the findings in Chapter III, they have concluded that adsorbates actively participate in corona formation with NPs, altering innate characteristics of the NPs by changing their surface chemistry.[38,76,92] There is remarkable agreement in the K_a values obtained through UV-Vis Langmuir isotherm technique and the novel NECEEM analysis, and zeta potential measurements confirm the formation of BSA and SRHA coronas. However, as a single adsorbate system is unlikely to be seen in the environmental settings, there is a dire need for developing model quantification methods for multi adsorbate systems.[32] Thus, in this chapter, a combination of qualitative analyses (DLS characterization and CD spectroscopy) and quantitative analysis (a novel CE-based pull-down assay) will be used to probe multi adsorbate systems under two different settings: competitive binding and sequential binding. The competitive binding system will shed light on how different adsorbates behave when encountered with bare AgNPs simultaneously, while sequential binding systems will probe how adsorbates react to pre-formed corona structures.

4.1.1 DLS Size and Zeta Potential Measurements

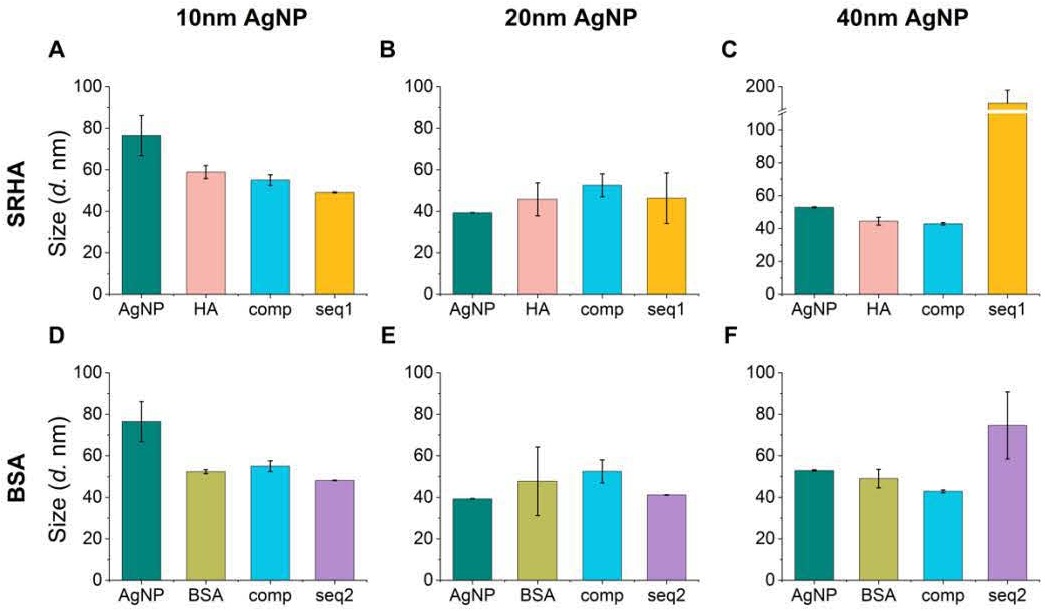

Figure 12. Effect of various incubation conditions on the hydrodynamic diameter of AgNPs. **(Top)** Effect of 60 mg L^{-1} SRHA on the diameter of **(A)** 10 nm **(B)** 20 nm **(C)** 40 nm AgNPs. **(Bottom)** Effect of 1 μM BSA on the diameter of **(D)** 10 nm **(E)** 20 nm **(F)** 40 nm AgNPs. AgNP denotes AgNPs prepared alone, (BSA and SRHA) denotes AgNPs prepared with either adsorbate, comp denotes AgNPs prepared simultaneously with SRHA and BSA, seq 1 denotes AgNPs sequentially incubated with BSA followed by SRHA, and seq 2 denotes AgNPs sequentially incubated with SRHA followed by BSA. All solutions contained 40 mg L^{-1} AgNPs in 10 mM sodium bicarbonate buffer solution (pH 7.0).

As with single adsorbate studies, DLS was used to measure the hydrodynamic diameter, PDI, and zeta potential of AgNPs resulting from each multi-adsorbate incubation (seq1, seq2, and comp). First, the adsorption of SRHA was probed for each of the multi-adsorbate conditions and compared to AgNPs alone or AgNPs with just SRHA (**Figure 12A-C**). For 10 and 20 nm AgNPs, subtle changes were shown in the hydrodynamic diameter when BSA and SRHA were added competitively or in sequence with 10 nm AgNPs generally showing a decrease in size and 20 nm AgNPs a slight increase in size (**Figure 12A,B**; see also **Figure A4, Table A5**). However, for the 40 nm AgNPs, a drastic increase in hydrodynamic size was shown when SRHA was added

sequentially (**Figure 12C**). Subtle decreases shown for competitive and sequential addition of SRHA for 10 nm AgNPs could be due to exchange of SRHA with BSA molecules in solution, or a more compact corona complex could have been formed through collaborative adsorption of BSA and SRHA. Subtle increases in size for 20 nm AgNPs in the competitive addition could be attributed to additional adsorption onto the AgNP surface with more adsorbates in solution. When SRHA is added sequentially, 20 nm AgNPs showed a similar trend as the 10 nm AgNPs in that the hydrodynamic size decreased slightly. It seems that adding in SRHA sequentially creates a more compact, ordered corona than in competitive addition formats. For the 40 nm AgNPs, competitive binding of BSA and SRHA showed a slight decrease from both AgNP only and AgNP with SRHA systems, indicating that there could be a more ordered corona for 40 nm AgNPs with additional adsorbates. When SRHA was added in sequentially, however, a palpable degree of aggregation was observed. This could be due to the fact that sequential addition of SRHA possibly creates a highly ordered corona complex with reduced distance between individual AgNPs. With individual AgNPs being closer to each other with shielded charge, the barrier to aggregation is overcome.

The adsorption of BSA was also probed for each of the multi adsorbate conditions against AgNP and AgNP with just BSA solutions (**Figure 12D-F**). For 10 and 20 nm AgNPs, competitive addition of BSA and SRHA seemed to slightly increase the hydrodynamic size of the AgNPs compared to just BSA. Sequential addition of BSA seemed to slightly decrease the size of the AgNPs for both 10 and 20 nm AgNPs, suggesting the idea that sequential addition of either adsorbate seems to form a more compact corona complex. For the 40 nm AgNPs, though, competitive addition of SRHA

and BSA decreased the hydrodynamic diameter while sequential addition of BSA caused aggregation, as was with sequential addition of SRHA. 40 nm AgNPs being specifically prone to aggregation compared to 10 and 20 nm AgNPs with sequential additions of either adsorbate could be due to the increased Van der Waals forces with increase in AgNP size. In addition, the decreased distance between individual AgNPs and the shielding of strong anionic charge on the AgNP surface makes the 40 nm AgNPs more susceptible to aggregation with sequential addition. It is interesting that competitive addition does not induce this type of aggregation, which could mean AgNP corona structures are more stable when AgNPs are interacting with a single adsorbate at a time, with or without pre-existing coronas.

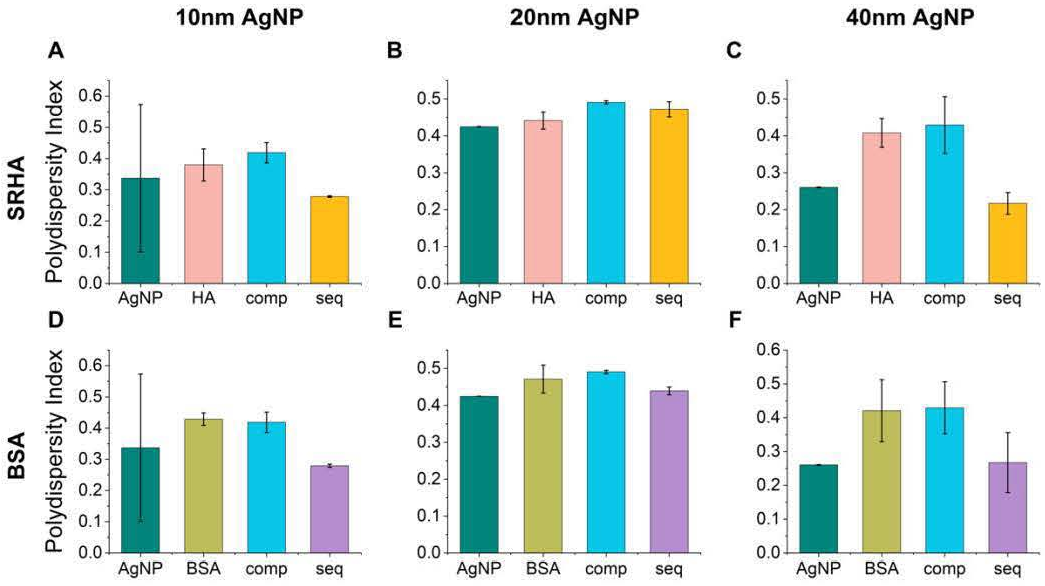

Figure 13. PDI of hydrodynamic diameter measurements of AgNPs under various incubation conditions. **(Top)** PDI of hydrodynamic diameter measurements showing effect of 60 mg L^{-1} SRHA on the diameter of **(A)** 10 nm **(B)** 20 nm **(C)** 40 nm AgNPs. **(Bottom)** PDI of hydrodynamic diameter measurements showing effect of 1 μM BSA on the diameter of **(D)** 10 nm **(E)** 20 nm **(F)** 40 nm AgNPs. AgNP denotes AgNPs prepared alone, (BSA and SRHA) denotes AgNPs prepared with either adsorbate, comp denotes AgNPs prepared simultaneously with SRHA and BSA, seq 1 denotes AgNPs sequentially incubated with BSA followed by SRHA, and seq 2 denotes AgNPs sequentially incubated with SRHA followed by BSA. All solutions contained 40 mg L^{-1} AgNPs in 10 mM sodium bicarbonate buffer solution (pH 7.0).

The PDI of all multi adsorbate hydrodynamic diameter measurements were also recorded (**Figure 13, Table A6**). Compared to AgNPs and AgNP with SRHA systems, the PDI of competitive binding systems slightly increased across all sizes (**Figure 13A-C**). For 10 nm and 40 nm AgNPs, sequential addition of SRHA decreased the PDI. For the 20 nm AgNPs, a small increase in PDI is evident from the single adsorbate system, but it is still smaller than the competitive system. A lower PDI in all sequential binding systems than competitive systems are interesting especially since sequential addition to 40 nm AgNPs induced aggregation. This would mean that 40 nm AgNPs are forming large but stable aggregates, which further corroborates the hypothesis that AgNP corona structures are more stable in sequential addition systems, regardless of aggregate formation. For BSA, a similar trend was shown (**Figure 13D-F**). A slight decrease in PDI was shown for the competitive binding system for 10 nm AgNPs compared to the single adsorbate system, while 20 and 40 nm AgNPs showed a subtle increase. These subtle changes from the single adsorbate system suggest that in competitive binding systems, the adsorbate with higher affinity is going to fully saturate the AgNP surface, without much of the other adsorbate participating in the corona. Throughout all three sizes, the PDI of the sequential addition of BSA decreased, with 10 and 40 nm AgNPs showing a larger decrease than the 20 nm AgNPs. This decrease highlights the stableness of AgNP corona structures in sequential binding systems, where sequential addition of BSA again showed increased aggregation in 40 nm AgNP systems.

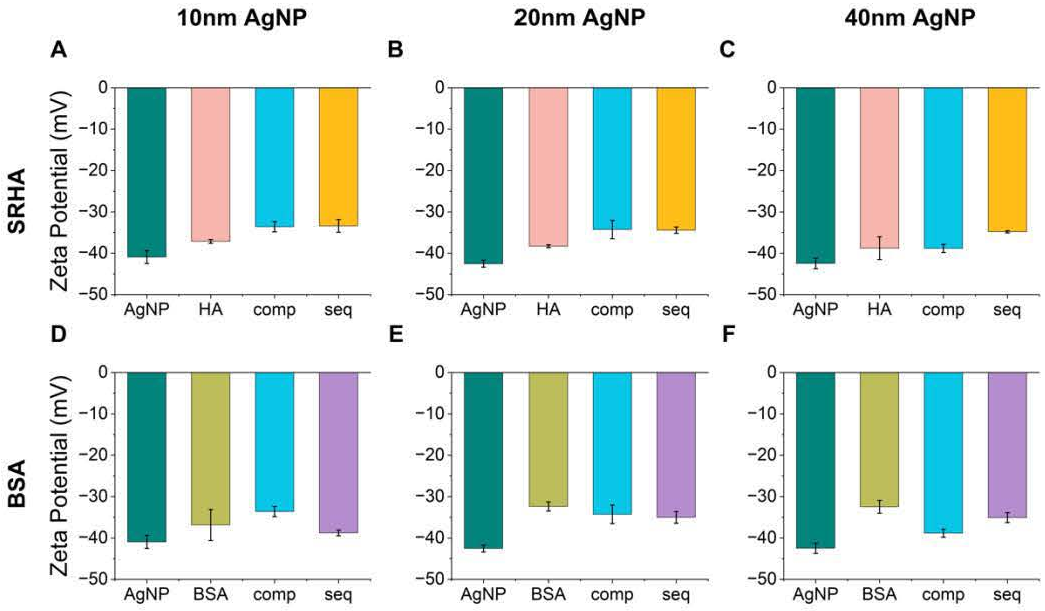

Figure 14. Effect of various incubation conditions on the zeta potentials of AgNPs. **(Top)** Effect of 60 mg L^{-1} SRHA on the zeta potential of **(A)** 10 nm **(B)** 20 nm **(C)** 40 nm AgNPs. **(Bottom)** Effect of 1 μM BSA on the zeta potential of **(D)** 10 nm **(E)** 20 nm **(F)** 40 nm AgNPs. AgNP denotes AgNPs prepared alone, (BSA and SRHA) denotes AgNPs prepared with either adsorbate, comp denotes AgNPs prepared simultaneously with SRHA and BSA, seq 1 denotes AgNPs sequentially incubated with BSA followed by SRHA, and seq 2 denotes AgNPs sequentially incubated with SRHA followed by BSA. All solutions contained 40 mg L^{-1} AgNPs in 10 mM sodium bicarbonate buffer solution (pH 7.0).

Finally, the zeta potentials of all muti adsorbate systems were also measured using DLS (**Figure 14, Table A7**). For all of the multi adsorbate conditions, the strong anionic charge of the AgNPs was shielded by the less anionic BSA and SRHA. First, adsorption of SRHA in multi adsorbate systems was compared to its single adsorbate and just AgNP systems (**Figure 13 A-C**). Competitive binding systems and sequential addition of SRHA both induced a slight increase in measured zeta potential for 10 and 20 nm AgNPs. This suggests that both BSA and SRHA are participating in corona formation with the AgNPs, as adsorption of the less anionic BSA caused a further increase in the zeta potential relative to just the SRHA corona. For 20 nm AgNPs, a similar trend is shown, but for 40 nm AgNPs, competitive binding shows no shift in zeta potential from

the SRHA only systems, while sequential addition of SRHA shows a slight increase in zeta potential. Perhaps the 40 nm AgNPs have more SRHA on the surface in competitive formats compared to sequential addition of SRHA, implying that displacement of adsorbates in the pre-formed corona complex is more difficult than when adsorbates are introduced simultaneously to the 40 nm AgNPs.

Multi adsorbate systems pertaining to BSA were also compared against just AgNP and AgNP with BSA as a single adsorbate system (**Figure 14D- F**). For the 10 nm AgNPs, competitive addition of both adsorbates showed an increase in zeta potential from when just BSA was added, suggesting that more BSA was adsorbed onto the 10 nm AgNPs in this format. Sequential addition of BSA then showed a slight decrease in zeta potential from the single adsorbate BSA system, further corroborating the idea that displacement of a pre-formed corona is harder than simple adsorption onto the bare AgNPs. For the 20 nm AgNPs, competitive addition of BSA and SRHA showed a slight decrease in zeta potential, showing that compared to the 10 nm AgNPs, more SRHA was incorporated into the corona structure when the adsorbates are added in simultaneously. The sequential addition of BSA shows a greater decrease in zeta potential, again due to displacement of a pre-formed corona having a larger energy barrier than simple adsorption onto bare AgNP surfaces. For the 40 nm AgNPs, sequential addition of BSA shows a decrease in zeta potential from the single adsorbate BSA system, but the competitive binding system shows yet a larger decrease in zeta potential. This points to the idea of 40 nm AgNPs having a higher affinity for SRHA than BSA, which is in direct contrast to the competitive binding system of the 10 nm AgNPs. Compiling all the data

together, it seems that the smaller AgNPs bind more favorably to the BSA, but as AgNP size gets larger, this preference shifts towards SRHA.

4.1.2 Semi-Quantitative Analysis of BSA Secondary Structure Using CD Spectroscopy

The changes to secondary structure of BSA in solution with AgNPs and in the presence of SRHA were measured using CD (**Figure 15**). As discussed previously, there was no significant difference in % α-helicity of BSA when incubated with differently sized AgNPs (**Figure 8**). However, when SRHA was added to the system of BSA and AgNPs either competitively or sequentially, the characteristic peak at 208 nm indicating the α-helicity of BSA significantly decreased in amplitude.

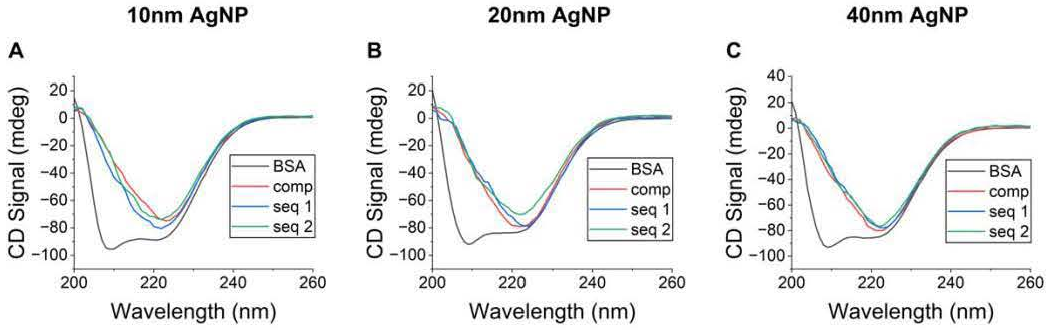

Figure 15. Overlay of CD spectra of BSA under various incubation conditions. **(A)** 10 nm **(B)** 20 nm, and **(C)** 40 nm AgNPs (40 mg L^{-1}) incubated with 1 μM BSA alone (BSA), with a mixture of 1 μM BSA and 60 mg L^{-1} SRHA (comp), with 1 μM BSA followed by 60 mg L^{-1} SRHA (seq 1), and with 60 mg L^{-1} SRHA followed by 1 μM BSA (seq 2).

The % α-helicity of the molecules in the samples were quantified using equation 8 (**Figure 16**). Regardless of the AgNP size, when SRHA is added to the system, BSA appears to lose all of its α helical nature. Previous literature suggests that BSA can unfold when adsorbed onto the AgNP surface.[93] However, as can be seen by the % α-helicity around 40% for BSA in the presence of all three sizes of AgNPs, the dramatic decrease

of % α-helicity in the competitive and sequential additions of BSA and SRHA can be attributed to SRHA inducing the unfolding of BSA in solution.

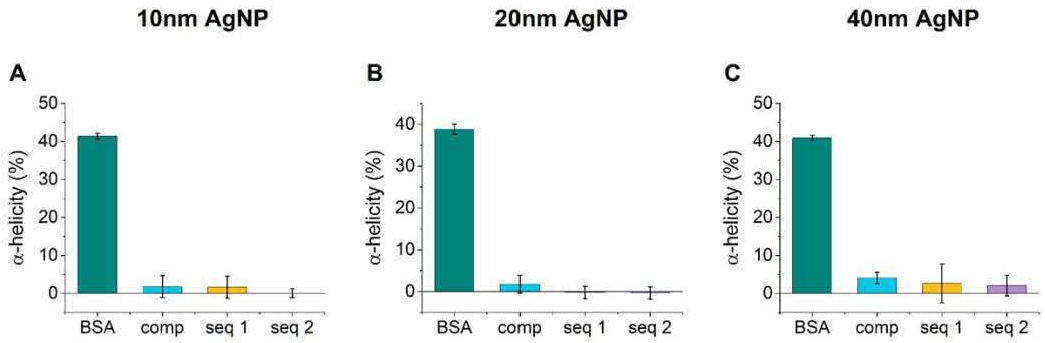

Figure 16. % α-helicity of all conditions. α-helicity calculated for 1 μM BSA (BSA), mixture of 1 μM BSA and 60 mg L^{-1} SRHA (comp), sequential addition of 24 hrs of incubation with BSA before addition of SRHA (seq 1), and sequential addition of 24 hrs of incubation with SRHA before addition of BSA (seq 2) prepared with 40 mg L^{-1} **(A)** 10 nm AgNPs **(B)** 20 nm AgNPs and **(C)** 40 nm AgNPs using equation 8.

To further investigate whether SRHA induced denaturation of BSA independent of the corona formation processes, CD measurements were recorded of 1 μM BSA in solution with 60 mg L^{-1} SRHA in the absence of AgNPs (**Figure 17A**). The observable decrease in % α-helicity in the solution containing both adsorbates is shown (**Figure 17B**). However, in the absence of AgNPs, the SRHA only induces a decrease in % α-helicity from 41.4% to 23.9% (**Table A4**). Thus, the BSA fully unfolding seems to be mediated by both AgNPs and SRHA. A combination of SRHA unfolding free BSA in solution and mediating conformational changes on BSA already adsorbed to the AgNP surface could explain why BSA undergoes full denaturation in the presence of both.

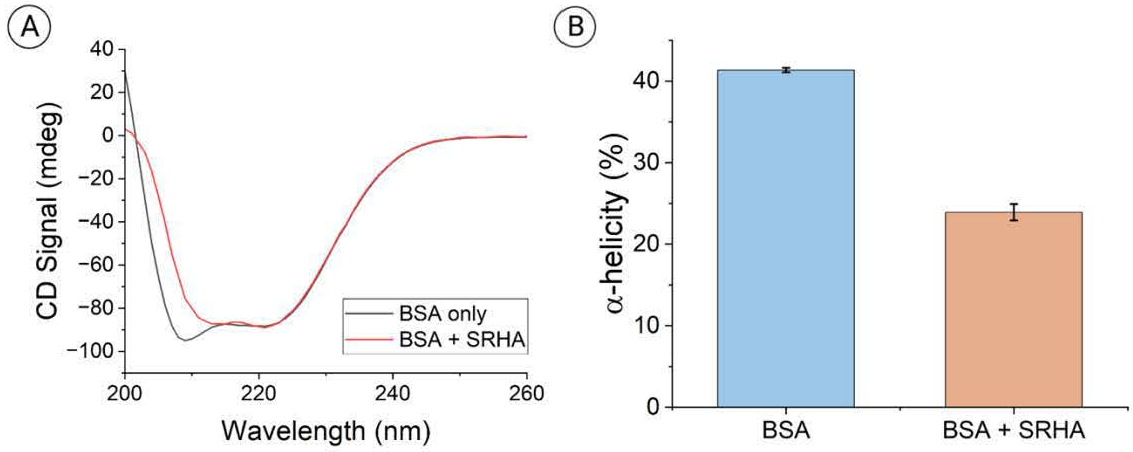

Figure 17. % α-helicity for Controls. **(A)** Overlay of CD spectra of 1 μM BSA without (BSA only) and with 60 mg L^{-1} SRHA (BSA + SRHA) after 24 hrs of incubation prepared in 10 mM sodium bicarbonate buffer (pH 7.0). **(B)** % α-helicity for both samples calculated using equation 8.

Overall, with DLS measurements, it was discovered that competitive adsorption systems generally provide more adsorption of BSA and SRHA than single adsorbate systems, and the smaller AgNPs favor BSA adsorption while the larger particles favor SRHA adsorption. For the sequential addition of adsorbates in either case, a deviation from the single adsorbate systems is evident, but the corona complex seems to retain some of the adsorbates added first into the AgNP solutions. The displacement of adsorbates participating in the pre-formed corona provides a higher energy barrier for sequentially added adsorbate binding to the AgNP surface than to bare AgNP surfaces. Also, BSA unfolding seems to be mediated not only by adsorption onto AgNP surfaces, but also by free SRHA in solution, as was shown by CD analyses. However, to fully understand and validate observations made through these qualitative analyses, quantitative assays such as the CE pull-down assay will need to be incorporated.

4.2 CE Pull-down Assay Principles

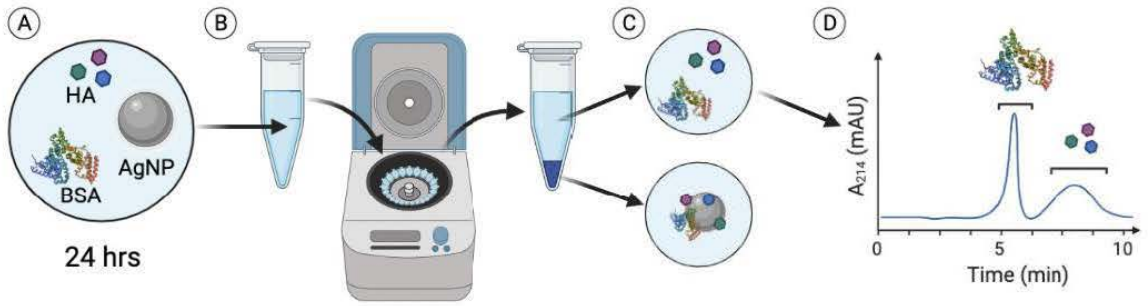

Figure 18. Schematic of the CE pull-down assay for quantifying competitive binding. **(A)** A mixture containing AgNPs with multiple adsorbates is incubated overnight and **(B)** centrifuged to separate bound and unbound adsorbates. **(C)** The supernatant containing unbound adsorbates is isolated and **(D)** analyzed using CE.

The CE pull-down assay is modeled after a traditional biochemical pull-down assay, taking advantage of the interactions between the adsorbates and the AgNPs to quantify the percentage of the adsorbates populating the corona.[94] The entire pull-down assay is outlined in **Figure 18**. First, BSA and SRHA are simultaneously pipetted into the pre-concentrated AgNP solutions. Then, all samples are incubated for 24 hrs to have the corona complexes reach equilibrium. The next day, centrifugation is used to pellet the AgNPs and any adsorbates on the surface, leaving unbound adsorbates in the supernatant. The supernatant is removed and injected into the CE where BSA and SRHA can be separated and quantified by comparison to calibration curves created the same day (**Figure 19**). Finally, using equation 9, the % bound of the BSA was determined.

$$\%\ Adsorbate_{bound} = \frac{[Adsorbate]_0 - [Adsorbate]_{sample}}{[Adsorbate]_0} \times 100 \qquad (9)$$

where $[Adsorbate]_0$ is the initial adsorbate concentration, and the $[Adsorbate]_{sample}$ is the concentration of the adsorbate following the pull-down assay procedure. The initial adsorbate concentration was determined using a control sample containing just 1 μM

BSA or a combination of 1 μM BSA and 60 mg L^{-1} SRHA prepared in 10 mM sodium bicarbonate (pH 7.0). Control samples went through all steps of the pull-down assay procedure, just as samples containing AgNPs, to eliminate the effect of nonspecific adsorption of adsorbates onto the plastic sample tubes.

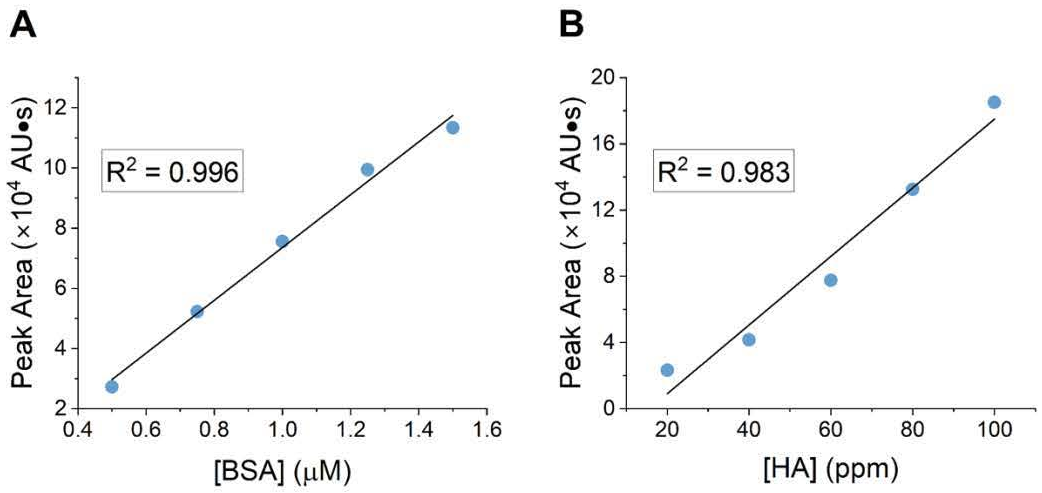

Figure 19. Representative calibration curves from the CE pull-down assay. **(A)** Calibration curve of BSA and **(B)** SRHA analyzed in a mixture. Five calibration standards were prepared containing mixtures of increasing concentrations of each adsorbated (BSA = 0.5, 0.75, 1.0, 1.25, or 1.5 μM and SRHA = 20, 40, 60, 80, or 100 mg L^{-1}).

4.3 Optimization of CE Separation Conditions

The success of the CE pull-down assay relies on the efficient separation of the components in the multi-adsorbate corona. Thus, experimental conditions for adequate separation between model adsorbates BSA and SRHA were optimized (**Figure 20**). A quality separation was determined through clear baseline resolution between the BSA peak and the SRHA peak. First, a mixture of BSA and SRHA was prepared in 25 mM of each of four different buffers – sodium phosphate, HEPES, sodium bicarbonate, and Tris

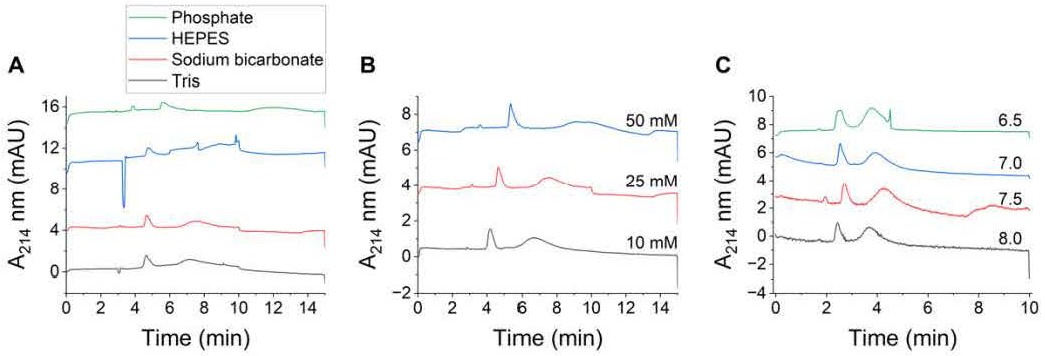

Figure 20. Optimization of separation conditions for the CE pull-down assay. Electropherograms of a mixture of 1 μM BSA and 60 mg L^{-1} SRHA prepared in **(A)** 25 mM sodium phosphate (pH 7.2), HEPES (pH 7.3), sodium bicarbonate (pH 8.3), and Tris buffer (pH 8.0), **(B)** 10, 25 and 50 mM sodium bicarbonate buffer (pH 8.3), and **(C)** 10 mM sodium bicarbonate buffer with a pH of 6.5, 7.0, 7.5 and 8.0.

(**Figure 20A**). Compared to the sodium bicarbonate and Tris buffers, the sodium phosphate and HEPES buffers did not provide a quality peak for either adsorbate. The peaks were asymmetric and had low signal intensity. Between Tris and sodium bicarbonate, we proceeded to optimize the conditions for the sodium bicarbonate buffer since it is more environmentally relevant. Then, the concentration of the buffer was investigated. Three different concentrations, 10, 25 and 50 mM, sodium bicarbonate buffer systems were probed (**Figure 20B**). Since all three concentrations of buffer provide adequate separation between the two peaks, the 10 mM sodium bicarbonate solution was chosen since it yielded sharper peaks and faster migration times, without any negative effects on peak resolution. Furthermore, the pH of the buffer also affects the separation of analytes in CE.[80] Thus, the pH of the 10 mM sodium bicarbonate solution was tuned to 6.5, 7.0, 7.5 or 8.0 from its inherent pH of 8.3 through dropwise addition of 1.0 and 0.1 M HCl (**Figure 20C**). It was found that at pH of 8.0, the BSA and SRHA peaks seemed to overlap slightly, and as the pH decreased, more separation was evident between the two peaks. However, when the pH reached 6.5, the BSA peak appeared less

sharp, and there was slight assymetry of the SRHA peak. Thus, the optimized buffer condition was 10 mM sodium bicarbonate buffer with a pH of 7.0.

In addition to optimizing the buffer conditions, the cross-sectional diameter of the capillary and the separation voltage were optimized. Capillaries with cross-sectional diameters of 75 μm and 50 μm were used, while the effective and total capillary length were kept constant at 50.0 and 60.2 cm, respectively. Capillaries with smaller inner diameters typically allow for better separation due to increased currents for the same applied voltage.[78] It was found that samples analyzed using a 75 μm capillary were not fully separated and had similar migration times (data not shown). Thus, the smaller capillary (50 μm) was chosen for this study. The separation voltage was also optimized. Higher voltages, and thus higher potential differences between electrodes, result in faster migration times, which can lead to sharper peaks and improved resolution. However, if the separation voltage is too high, the BSA and SRHA molecules do not have sufficient time to separate based on their electrophoretic mobilities and the peaks could overlap. On the other hand, with too low of a voltage, the analysis time becomes too slow and peak broadening can lead to overlapping peaks and larger errors in quantification of peak intensities. Thus, voltages of 25 kV and 20 kV were probed to ensure the full separation between SRHA and BSA, while also maintaining the integrity of their individual peaks. A potential difference of 25 kV allowed the samples to migrate through the capillary faster, and there was still clear separation between SRHA and BSA, so 25 kV was used as the potential difference between the electrodes for this study.

4.4 Application of the CE Pull-down Assay to Quantify Formation of Multi-Adsorbate Coronas

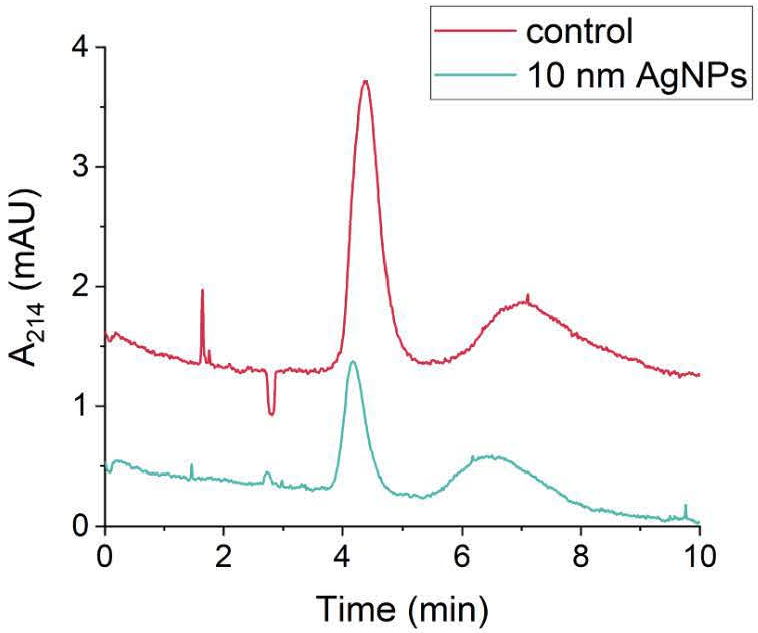

Figure 21. Characteristic electropherograms obtained from the pull-down assay. Electropherogram plotting the absorbance at 214 nm for a mixture of 60 mg L^{-1} SRHA and 1 μM BSA prepared in 10 mM sodium bicarbonate (pH 7.0) buffer (control) and the same mixture in the presence of 40 mg L^{-1} 10 nm AgNPs after the pull-down procedure (10 nm AgNPs).

With the optimization of the CE conditions completed, preliminary studies were conducted to evaluate how adsorption of BSA was mediated by the addition of SRHA into the system. BSA was incubated with pre-concentrated AgNPs of different sizes with and without SRHA competitively mixed in solution. All values of % BSA bound were normalized against a control sample of just BSA in sodium bicarbonate buffer or a mixture containing just BSA and SRHA in the same buffer to account for non-specific adsorption to the plastic Eppendorf tubes used for overnight sample incubation (**Figure 21**). Across all AgNP sizes, BSA adsorption to AgNPs slightly decreased with the addition of SRHA (**Figure 22A**). This indicates that there is binding of both adsorbates onto the AgNP surface, and some binding sites are blocked by adsorption of SRHA,

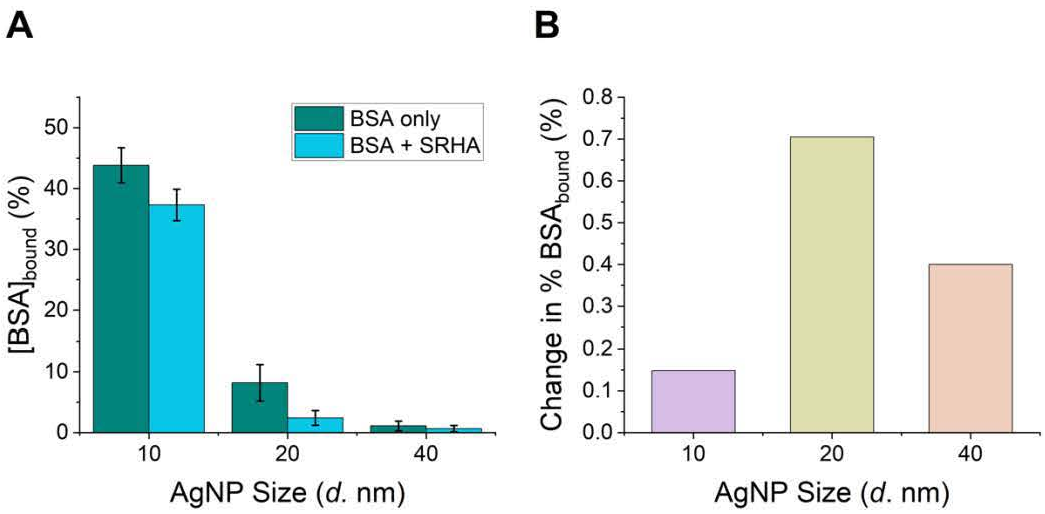

Figure 22. % BSA bound mediated by competitive addition of SRHA. **(A)** Percentage of BSA adsorbed to AgNPs in the absence or presence of SRHA determined by the CE pull-down assay. The percentage of BSA bound was determined for solutions of 40 mg L^{-1} 10, 20, and 40 nm AgNPs incubated with 1 μM BSA alone (BSA only) or a mixture of 1 μM BSA and 60 mg L^{-1} SRHA. **(B)** Effect of competitively adding SRHA in % BSA bound for 10, 20 and 40 nm AgNP solutions.

lowering the % bound of the BSA. In addition, with the addition of SRHA into the system, denaturation of the unbound BSA, which was shown in CD analyses, could have altered it to a state now unable to bind to AgNP surfaces. The change in % BSA bound after addition of SRHA was also calculated through comparison of the BSA only system and the system with competitive addition of BSA and SRHA (**Figure 22B, Table A8**). Although 10 nm AgNPs had the largest % BSA bound in the system, they also had the smallest change in % BSA bound after addition of SRHA into the system. There was an increase in change in % BSA bound for 40 nm AgNPs and the 20 nm AgNPs had the largest change in % BSA bound. The small initial % bound of the 20 nm and 40 nm AgNPs could have skewed the change in % BSA bound. But the larger change in % BSA bound for the 20 and 40 nm AgNPs is in great agreement with the observation from the qualitative analyses: larger AgNPs have a higher binding affinity for SRHA, while 10 nm AgNPs favor BSA binding.

Overall, the pull-down assay was shown to effectively probe multi adsorbate systems by indicating a change in % BSA bound when SRHA was added into the system. The results from the quantitative analyses aligning well with the qualitative observations is a good indicator of validation for this novel technique, and hopefully the pull-down assay can be used to probe binding activity of different, more environmentally relevant proteins with the AgNPs in the future.

Chapter V: Conclusions and Future Directions

As aforementioned, protein coronas greatly alter AgNP behaviors within an organism or an ecosystem, including their adsorption, distribution, biotransformation and fate.[32] Protein coronas have asserted themselves as major constituents in treating diseases in medical settings, such as assisting in drug delivery,[2] inducing apoptosis in cancer cells, and allowing interactions with other cellular sites that bare AgNPs cannot access.[76] AgNP-PCs can evade the immune system by having the corona be constituted of specific proteins that are prevalent in the body and would help the AgNPs circumvent opsonization. By loading ligands that specifically bind to target cells of concern, AgNP-PCs can also be used to deliver drugs to target cells.[2] While studies indicate that the structure of the NPs itself also seems to have an impact on the ability to evade the immune system of the NP-PC complex that follows,[95] protein composition of the PC is deemed to most significant factor. Thus, development of quantitative analyses that can enhance our understanding of these corona structures is essential.

In this work, two novel CE techniques, NECEEM and the pull-down assay, were developed and validated for quantitative analyses on both single and multi-adsorbate systems. Qualitative analyses – namely, DLS and CD – were also employed to provide adequate support for results obtained through the quantitative analyses. The primary findings are, in accord with previous literature, the size of the AgNP directs their reactivity with adsorbates, with specific sizes favoring one adsorbate over the other. Further, an interesting finding from this work was the altered binding behavior and changes in secondary structure of BSA induced by the addition of SRHA into the system.

In the foreseeable future, optimization of NECEEM conditions to analyze SRHA-AgNP complexes will have to be performed to compare with UV-Vis Langmuir isotherms to further validate the NECEEM technique. More work on the SRHA portion of the pull-down assay will also have to be performed to study how its binding behaviors are altered by BSA. Moreover, the pull-down assay has only been applied to competitive binding scenarios to date, so future work will seek to quantify the effects of sequential additions of BSA and SRHA on their binding affinity. Results from qualitative analyses suggest some changes to the structure of the corona depending on the adsorption conditions with some conditions leading to the formation of compact coronas and others leading to AgNP aggregation. To affirm these hypotheses, all samples studied in the single and multi-adsorbate scenarios will be imaged with TEM to visualize the corona. Then, the TEM images will be correlated with DLS size data obtained through this work to further investigate corona formation mechanisms qualitatively.

Other studies in the literature have shown that the adsorption of proteins onto the AgNP surface can restructure the surface chemistry of AgNPs, possibly opening binding sites previously inaccessible.[3,35] Thus, once the pull-down assay is fully optimized, a natural extension of this work would be its application to complex coronas containing more than two adsorbates. Specifically, with a focus on the application of AgNPs in medicine, more biologically relevant proteins can be studied to understand how binding behaviors are mediated through protein-protein interactions. For example, serum proteins such as fibrinogen, human serum albumin, immunoglobulin G and α2HS glycoprotein, could be useful to study due to their different sizes, charge, and functions. Interestingly, fibrinogen and immunoglobulin G were recently shown to work cooperatively to adsorb

to NP surfaces.[35] The pull-down assay could provide interesting insights to this PC system.

Acknowledgements

I would like to start off by thanking everyone in the Riley lab during my long tenure working in this lab. Thanks to all the members from my first year in lab – Zac O'Dell, Janan Hui, Dan Boehmler, Hee Yon Park and Maddie Farber – for making my first year in the lab delightful and creating a working atmosphere where everyone is welcomed. During the Covid years, thank you to Carole Lee, Marcos Estrada and Tolu Banjo for keeping by my side on Zoom, even though I was halfway across the world. Thank you to the members in my last year of lab for making the transition back into education bearable after a two-year hiatus in the military. It was really enjoyable to share the same space with Mary Garcia-Barros and Michael Caprise, the microplastics dream team, Casey Jordan, the pitcher who let me hit bombs off of him, Tim Kihiczak, the guy who lives in the matchbox, and Maddie Farber, the person who shared my long journey in this lab together from start to finish.

I want to especially thank Doctor Kathryn Riley for being the best PI anyone could ask for. She is a superhuman who always knows what to do, and she has been a great mentor for me not just in research, but also in life. Thank you for bringing the senior citizen back into lab and helping me in every way at Swarthmore, from when I was a lost sophomore to now, a lost senior about to graduate.

I would also like to thank the whole Swarthmore Chemistry Department for funding and guiding me throughout my whole journey at Swarthmore, especially the members of my committee, Professor Emily Sahadeo, Professor Kathryn Riley, and Professor Kathleen Howard, for reading and critiquing my work. And of course, a huge thank you to Sumin Byun for giving me everything I needed when I needed it most.

References

(1) Nowack, B.; Krug, H. F.; Height, M. 120 Years of Nanosilver History: Implications for Policy Makers. *Environ. Sci. Technol.* **2011**, *45* (4), 1177–1183. https://doi.org/10.1021/es103316q.

(2) Corbo, C.; Molinaro, R.; Parodi, A.; Toledano Furman, N. E.; Salvatore, F.; Tasciotti, E. The Impact of Nanoparticle Protein Corona on Cytotoxicity, Immunotoxicity and Target Drug Delivery. *Nanomed.* **2016**, *11* (1), 81–100. https://doi.org/10.2217/nnm.15.188.

(3) Ju, Y.; Kelly, H. G.; Dagley, L. F.; Reynaldi, A.; Schlub, T. E.; Spall, S. K.; Bell, C. A.; Cui, J.; Mitchell, A. J.; Lin, Z.; Wheatley, A. K.; Thurecht, K. J.; Davenport, M. P.; Webb, A. I.; Caruso, F.; Kent, S. J. Person-Specific Biomolecular Coronas Modulate Nanoparticle Interactions with Immune Cells in Human Blood. *ACS Nano* **2020**, *14* (11), 15723–15737. https://doi.org/10.1021/acsnano.0c06679.

(4) Cox, A.; Andreozzi, P.; Dal Magro, R.; Fiordaliso, F.; Corbelli, A.; Talamini, L.; Chinello, C.; Raimondo, F.; Magni, F.; Tringali, M.; Krol, S.; Jacob Silva, P.; Stellacci, F.; Masserini, M.; Re, F. Evolution of Nanoparticle Protein Corona across the Blood–Brain Barrier. *ACS Nano* **2018**, *12* (7), 7292–7300. https://doi.org/10.1021/acsnano.8b03500.

(5) Wang, F.; Chen, Z.; Wang, Y.; Ma, C.; Bi, L.; Song, M.; Jiang, G. Silver Nanoparticles Induce Apoptosis in HepG2 Cells through Particle-Specific Effects on Mitochondria. *Environ. Sci. Technol.* **2022**. https://doi.org/10.1021/acs.est.1c08246.

(6) Keller, A. A.; McFerran, S.; Lazareva, A.; Suh, S. Global Life Cycle Releases of Engineered Nanomaterials. *J. Nanoparticle Res.* **2013**, *15* (6), 1–17.

(7) Shafer, M. M.; Hoffmann, S. R.; Overdier, J. T.; Armstrong, D. E. Physical and Kinetic Speciation of Copper and Zinc in Three Geochemically Contrasting Marine Estuaries. *Environ. Sci. Technol.* **2004**, *38* (14), 3810–3819. https://doi.org/10.1021/es0306765.

(8) Brar, S. K.; Verma, M.; Tyagi, R. D.; Surampalli, R. Y. Engineered Nanoparticles in Wastewater and Wastewater Sludge – Evidence and Impacts. *Waste Manag.* **2010**, *30* (3), 504–520. https://doi.org/10.1016/j.wasman.2009.10.012.

(9) Azodi, M.; Sultan, Y.; Ghoshal, S. Dissolution Behavior of Silver Nanoparticles and Formation of Secondary Silver Nanoparticles in Municipal Wastewater by Single-Particle ICP-MS. *Environ. Sci. Technol.* **2016**, *50* (24), 13318–13327. https://doi.org/10.1021/acs.est.6b03957.

(10) Kim, B.; Park, C.-S.; Murayama, M.; Hochella, M. F. Discovery and Characterization of Silver Sulfide Nanoparticles in Final Sewage Sludge Products. *Environ. Sci. Technol.* **2010**, *44* (19), 7509–7514. https://doi.org/10.1021/es101565j.

(11) Steinhoff, B.; Müller, J.; Mozhayeva, D.; Spelz, B. T. F.; Engelhard, C.; Butz, B.; Schönherr, H. Investigation of the Fate of Silver and Titanium Dioxide Nanoparticles in Model Wastewater Effluents via Selected Area Electron Diffraction. *Environ. Sci. Technol.* **2020**, *54* (14), 8681–8689. https://doi.org/10.1021/acs.est.9b07840.

(12) Unrine, J. M.; Hunyadi, S. E.; Tsyusko, O. V.; Rao, W.; Shoults-Wilson, W. A.; Bertsch, P. M. Evidence for Bioavailability of Au Nanoparticles from Soil and Biodistribution within Earthworms (*Eisenia Fetida*). *Environ. Sci. Technol.* **2010**, *44* (21), 8308–8313. https://doi.org/10.1021/es101885w.
(13) Louie, S. M.; Ma, R.; Lowry, G. V. Transformations of Nanomaterials in the Environment. In *Frontiers of Nanoscience*; Elsevier, 2014; Vol. 7, pp 55–87. https://doi.org/10.1016/B978-0-08-099408-6.00002-5.
(14) Quadros, M. E.; Pierson, R.; Tulve, N. S.; Willis, R.; Rogers, K.; Thomas, T. A.; Marr, L. C. Release of Silver from Nanotechnology-Based Consumer Products for Children. *Environ. Sci. Technol.* **2013**, *47* (15), 8894–8901. https://doi.org/10.1021/es4015844.
(15) Mackevica, A.; Olsson, M. E.; Hansen, S. F. The Release of Silver Nanoparticles from Commercial Toothbrushes. *J. Hazard. Mater.* **2017**, *322*, 270–275. https://doi.org/10.1016/j.jhazmat.2016.03.067.
(16) Potter, P. M.; Navratilova, J.; Rogers, K. R.; Al-Abed, S. R. Transformation of Silver Nanoparticle Consumer Products during Simulated Usage and Disposal. *Environ. Sci. Nano* **2019**, *6* (2), 592–598.
(17) Benn, T. M.; Westerhoff, P. Nanoparticle Silver Released into Water from Commercially Available Sock Fabrics. *Environ. Sci. Technol.* **2008**, *42* (11), 4133–4139. https://doi.org/10.1021/es7032718.
(18) Mariano, S.; Panzarini, E.; Inverno, M. D.; Voulvoulis, N.; Dini, L. Toxicity, Bioaccumulation and Biotransformation of Glucose-Capped Silver Nanoparticles in Green Microalgae Chlorella Vulgaris. *Nanomaterials* **2020**, *10* (7), 1377. https://doi.org/10.3390/nano10071377.
(19) Kinaret, P.; Ilves, M.; Fortino, V.; Rydman, E.; Karisola, P.; Lähde, A.; Koivisto, J.; Jokiniemi, J.; Wolff, H.; Savolainen, K.; Greco, D.; Alenius, H. Inhalation and Oropharyngeal Aspiration Exposure to Rod-Like Carbon Nanotubes Induce Similar Airway Inflammation and Biological Responses in Mouse Lungs. *ACS Nano* **2017**, *11* (1), 291–303. https://doi.org/10.1021/acsnano.6b05652.
(20) Pietroiusti, A.; Stockmann-Juvala, H.; Lucaroni, F.; Savolainen, K. Nanomaterial Exposure, Toxicity, and Impact on Human Health. *WIREs Nanomedicine Nanobiotechnology* **2018**, *10* (5). https://doi.org/10.1002/wnan.1513.
(21) Rossi, E. M.; Pylkkänen, L.; Koivisto, A. J.; Nykäsenoja, H.; Wolff, H.; Savolainen, K.; Alenius, H. Inhalation Exposure to Nanosized and Fine TiO2 Particles Inhibits Features of Allergic Asthma in a Murine Model. *Part. Fibre Toxicol.* **2010**, *7* (1), 35. https://doi.org/10.1186/1743-8977-7-35.
(22) Hadrup, N.; Lam, H. R. Oral Toxicity of Silver Ions, Silver Nanoparticles and Colloidal Silver – A Review. *Regul. Toxicol. Pharmacol.* **2014**, *68* (1), 1–7. https://doi.org/10.1016/j.yrtph.2013.11.002.
(23) Antony, J. J.; Sivalingam, P.; Chen, B. Toxicological Effects of Silver Nanoparticles. *Environ. Toxicol. Pharmacol.* **2015**, *40* (3), 729–732. https://doi.org/10.1016/j.etap.2015.09.003.
(24) Siddiqi, K. S.; Husen, A.; Rao, R. A. K. A Review on Biosynthesis of Silver Nanoparticles and Their Biocidal Properties. *J. Nanobiotechnology* **2018**, *16* (1), 14. https://doi.org/10.1186/s12951-018-0334-5.

(25) Huang, M.; Keller, A. A.; Wang, X.; Tian, L.; Wu, B.; Ji, R.; Zhao, L. Low Concentrations of Silver Nanoparticles and Silver Ions Perturb the Antioxidant Defense System and Nitrogen Metabolism in N 2 -Fixing Cyanobacteria. *Environ. Sci. Technol.* **2020**, *54* (24), 15996–16005. https://doi.org/10.1021/acs.est.0c05300.
(26) Bao, S.; Xue, L.; Xiang, D.; Xian, B.; Tang, W.; Fang, T. Silver Nanoparticles Alter the Bacterial Assembly and Antibiotic Resistome in Biofilm during Colonization. *Environ. Sci. Nano* **2023**, *10* (2), 656–671. https://doi.org/10.1039/D2EN01018F.
(27) Zhang, H.; Huang, M.; Zhang, W.; Gardea-Torresdey, J. L.; White, J. C.; Ji, R.; Zhao, L. Silver Nanoparticles Alter Soil Microbial Community Compositions and Metabolite Profiles in Unplanted and Cucumber-Planted Soils. *Environ. Sci. Technol.* **2020**, *54* (6), 3334–3342. https://doi.org/10.1021/acs.est.9b07562.
(28) Forstner, C.; Orton, T. G.; Wang, P.; Kopittke, P. M.; Dennis, P. G. Wastewater Treatment Processing of Silver Nanoparticles Strongly Influences Their Effects on Soil Microbial Diversity. *Environ. Sci. Technol.* **2020**, *54* (21), 13538–13547. https://doi.org/10.1021/acs.est.0c01312.
(29) Pino, P. del; Pelaz, B.; Zhang, Q.; Maffre, P.; Nienhaus, G. U.; Parak, W. J. Protein Corona Formation around Nanoparticles – from the Past to the Future. *Mater Horiz* **2014**, *1* (3), 301–313. https://doi.org/10.1039/C3MH00106G.
(30) Podila, R.; Chen, R.; Ke, P. C.; Brown, J. M.; Rao, A. M. Effects of Surface Functional Groups on the Formation of Nanoparticle-Protein Corona. *Appl. Phys. Lett.* **2012**, *101* (26), 263701. https://doi.org/10.1063/1.4772509.
(31) Shannahan, J. The Biocorona: A Challenge for the Biomedical Application of Nanoparticles. *Nanotechnol. Rev.* **2017**, *6* (4), 345–353. https://doi.org/10.1515/ntrev-2016-0098.
(32) Wheeler, K. E.; Chetwynd, A. J.; Fahy, K. M.; Hong, B. S.; Tochihuitl, J. A.; Foster, L. A.; Lynch, I. Environmental Dimensions of the Protein Corona. *Nat. Nanotechnol.* **2021**, *16* (6), 617–629. https://doi.org/10.1038/s41565-021-00924-1.
(33) Cedervall, T.; Lynch, I.; Lindman, S.; Berggård, T.; Thulin, E.; Nilsson, H.; Dawson, K. A.; Linse, S. Understanding the Nanoparticle–Protein Corona Using Methods to Quantify Exchange Rates and Affinities of Proteins for Nanoparticles. *Proc. Natl. Acad. Sci.* **2007**, *104* (7), 2050–2055. https://doi.org/10.1073/pnas.0608582104.
(34) Westmeier, D.; Stauber, R. H.; Docter, D. The Concept of Bio-Corona in Modulating the Toxicity of Engineered Nanomaterials (ENM). *Toxicol. Appl. Pharmacol.* **2016**, *299*, 53–57. https://doi.org/10.1016/j.taap.2015.11.008.
(35) Zhang, Y.; Wu, J. L. Y.; Lazarovits, J.; Chan, W. C. W. An Analysis of the Binding Function and Structural Organization of the Protein Corona. *J. Am. Chem. Soc.* **2020**, *142* (19), 8827–8836. https://doi.org/10.1021/jacs.0c01853.
(36) Cai, R.; Ren, J.; Guo, M.; Wei, T.; Liu, Y.; Xie, C.; Zhang, P.; Guo, Z.; Chetwynd, A. J.; Ke, P. C.; Lynch, I.; Chen, C. Dynamic Intracellular Exchange of Nanomaterials' Protein Corona Perturbs Proteostasis and Remodels Cell Metabolism. *Proc. Natl. Acad. Sci.* **2022**, *119* (23), e2200363119. https://doi.org/10.1073/pnas.2200363119.
(37) Mu, Q.; Jiang, G.; Chen, L.; Zhou, H.; Fourches, D.; Tropsha, A.; Yan, B. Chemical Basis of Interactions Between Engineered Nanoparticles and Biological Systems. *Chem. Rev.* **2014**, *114* (15), 7740–7781. https://doi.org/10.1021/cr400295a.

(38) Melby, E. S.; Allen, C.; Foreman-Ortiz, I. U.; Caudill, E. R.; Kuech, T. R.; Vartanian, A. M.; Zhang, X.; Murphy, C. J.; Hernandez, R.; Pedersen, J. A. Peripheral Membrane Proteins Facilitate Nanoparticle Binding at Lipid Bilayer Interfaces. *Langmuir* **2018**, *34* (36), 10793–10805. https://doi.org/10.1021/acs.langmuir.8b02060.
(39) Melby, E. S.; Lohse, S. E.; Park, J. E.; Vartanian, A. M.; Putans, R. A.; Abbott, H. B.; Hamers, R. J.; Murphy, C. J.; Pedersen, J. A. Cascading Effects of Nanoparticle Coatings: Surface Functionalization Dictates the Assemblage of Complexed Proteins and Subsequent Interaction with Model Cell Membranes. *ACS Nano* **2017**, *11* (6), 5489–5499. https://doi.org/10.1021/acsnano.7b00231.
(40) Wang, C.; Chen, B.; He, M.; Hu, B. Composition of Intracellular Protein Corona around Nanoparticles during Internalization. *ACS Nano* **2021**, *15* (2), 3108–3122. https://doi.org/10.1021/acsnano.0c09649.
(41) Fadare, O. O.; Wan, B.; Liu, K.; Yang, Y.; Zhao, L.; Guo, L.-H. Eco-Corona vs Protein Corona: Effects of Humic Substances on Corona Formation and Nanoplastic Particle Toxicity in *Daphnia Magna*. *Environ. Sci. Technol.* **2020**, *54* (13), 8001–8009. https://doi.org/10.1021/acs.est.0c00615.
(42) Liu, S.; Junaid, M.; Liao, H.; Liu, X.; Wu, Y.; Wang, J. Eco-Corona Formation and Associated Ecotoxicological Impacts of Nanoplastics in the Environment. *Sci. Total Environ.* **2022**, *836*, 155703. https://doi.org/10.1016/j.scitotenv.2022.155703.
(43) Natarajan, L.; Jenifer, M. A.; Mukherjee, A. Eco-Corona Formation on the Nanomaterials in the Aquatic Systems Lessens Their Toxic Impact: A Comprehensive Review. *Environ. Res.* **2021**, *194*, 110669. https://doi.org/10.1016/j.envres.2020.110669.
(44) Levard, C.; Hotze, E. M.; Lowry, G. V.; Brown, G. E. Environmental Transformations of Silver Nanoparticles: Impact on Stability and Toxicity. *Environ. Sci. Technol.* **2012**, *46* (13), 6900–6914. https://doi.org/10.1021/es2037405.
(45) Zhang, J.; Guo, W.; Li, Q.; Wang, Z.; Liu, S. The Effects and the Potential Mechanism of Environmental Transformation of Metal Nanoparticles on Their Toxicity in Organisms. *Environ. Sci. Nano* **2018**, *5* (11), 2482–2499. https://doi.org/10.1039/C8EN00688A.
(46) Abbas, Q.; Yousaf, B.; Amina; Ali, M. U.; Munir, M. A. M.; El-Naggar, A.; Rinklebe, J.; Naushad, M. Transformation Pathways and Fate of Engineered Nanoparticles (ENPs) in Distinct Interactive Environmental Compartments: A Review. *Environ. Int.* **2020**, *138*, 105646. https://doi.org/10.1016/j.envint.2020.105646.
(47) Durán, N.; Silveira, C. P.; Durán, M.; Martinez, D. S. T. Silver Nanoparticle Protein Corona and Toxicity: A Mini-Review. *J. Nanobiotechnology* **2015**, *13*. https://doi.org/10.1186/s12951-015-0114-4.
(48) Wang, Q.; Lim, M.; Liu, X.; Wang, Z.; Chen, K. L. Influence of Solution Chemistry and Soft Protein Coronas on the Interactions of Silver Nanoparticles with Model Biological Membranes. *Environ. Sci. Technol.* **2016**, *50* (5), 2301–2309. https://doi.org/10.1021/acs.est.5b04694.
(49) Cui, Q.; Hernandez, R.; Mason, S. E.; Frauenheim, T.; Pedersen, J. A.; Geiger, F. Sustainable Nanotechnology: Opportunities and Challenges for

Theoretical/Computational Studies. *J. Phys. Chem. B* **2016**, *120* (30), 7297–7306. https://doi.org/10.1021/acs.jpcb.6b03976.
(50) Yan, N.; Wang, W.-X. Novel Imaging of Silver Nanoparticle Uptake by a Unicellular Alga and Trophic Transfer to Daphnia Magna. *Environ. Sci. Technol.* **2021**, *55* (8), 5143–5151. https://doi.org/10.1021/acs.est.0c08588.
(51) Findlay, M. R.; Freitas, D. N.; Mobed-Miremadi, M.; Wheeler, K. E. Machine Learning Provides Predictive Analysis into Silver Nanoparticle Protein Corona Formation from Physicochemical Properties. *Environ. Sci. Nano* **2018**, *5* (1), 64–71. https://doi.org/10.1039/C7EN00466D.
(52) Park, H.-Y.; Chung, C.; Eiken, M. K.; Baumgartner, K. V.; Fahy, K. M.; Leung, K. Q.; Bouzos, E.; Asuri, P.; Wheeler, K. E.; Riley, K. R. Silver Nanoparticle Interactions with Glycated and Non-Glycated Human Serum Albumin Mediate Toxicity. *Front. Toxicol.* **2023**, *5*, 1081753. https://doi.org/10.3389/ftox.2023.1081753.
(53) Grover, A.; Sinha, R.; Jyoti, D.; Faggio, C. Imperative Role of Electron Microscopy in Toxicity Assessment: A Review. *Microsc. Res. Tech.* **2022**, *85* (5), 1976–1989. https://doi.org/10.1002/jemt.24029.
(54) Li, J.; Xu, J.; Li, B.; He, L.; Lin, H.; Li, H.-W.; Shao, H. Advanced SEM and TEM Techniques Applied in Mg-Based Hydrogen Storage Research. *Scanning* **2018**, *2018*, 1–12. https://doi.org/10.1155/2018/6057496.
(55) Jafari Eskandari, M.; Gostariani, R.; Asadi Asadabad, M. Transmission Electron Microscopy of Nanomaterials. In *Electron Crystallography*; Singh, D., Condurache-Bota, S., Eds.; IntechOpen, 2020. https://doi.org/10.5772/intechopen.92212.
(56) Zaitun Hasibuan, P. A.; Yuandani; Tanjung, M.; Gea, S.; Pasaribu, K. M.; Harahap, M.; Perangin-Angin, Y. A.; Prayoga, A.; Ginting, J. G. Antimicrobial and Antihemolytic Properties of a CNF/AgNP-Chitosan Film: A Potential Wound Dressing Material. *Heliyon* **2021**, *7* (10), e08197. https://doi.org/10.1016/j.heliyon.2021.e08197.
(57) Fouad, H.; Yang, G.; El-Sayed, A. A.; Mao, G.; Khalafallah, D.; Saad, M.; Ga'al, H.; Ibrahim, E.; Mo, J. Green Synthesis of AgNP–Ligand Complexes and Their Toxicological Effects on Nilaparvata Lugens. *J. Nanobiotechnology* **2021**, *19* (1), 318. https://doi.org/10.1186/s12951-021-01068-z.
(58) Zhang, T.; Lu, D.; Zeng, L.; Yin, Y.; He, Y.; Liu, Q.; Jiang, G. Role of Secondary Particle Formation in the Persistence of Silver Nanoparticles in Humic Acid Containing Water under Light Irradiation. *Environ. Sci. Technol.* **2017**, *51* (24), 14164–14172. https://doi.org/10.1021/acs.est.7b04115.
(59) Andrews, S. S.; Tretton, J. Physical Principles of Circular Dichroism. *J. Chem. Educ.* **2020**, *97* (12), 4370–4376. https://doi.org/10.1021/acs.jchemed.0c01061.
(60) Keiderling, T. Instrumentation for Vibrational Circular Dichroism Spectroscopy: Method Comparison and Newer Developments. *Molecules* **2018**, *23* (9), 2404. https://doi.org/10.3390/molecules23092404.
(61) Quesada-Moreno, M. M.; Virgili, A.; Monteagudo, E.; Claramunt, R. M.; Avilés-Moreno, J. R.; López-González, J. J.; Alkorta, I.; Elguero, J. A Vibrational Circular Dichroism (VCD) Methodology for the Measurement of Enantiomeric Excess in Chiral Compounds in the Solid Phase and for the Complementary Use of NMR and

VCD Techniques in Solution: The Camphor Case. *The Analyst* **2018**, *143* (6), 1406–1416. https://doi.org/10.1039/C7AN01855J.
(62) Stephens, P. J. Theory of Vibrational Circular Dichroism. *J. Phys. Chem.* **1985**, *89* (5), 748–752. https://doi.org/10.1021/j100251a006.
(63) Greenfield, N. J. Using Circular Dichroism Spectra to Estimate Protein Secondary Structure. *Nat. Protoc.* **2006**, *1* (6), 2876–2890. https://doi.org/10.1038/nprot.2006.202.
(64) Buckley, A.; Warren, J.; Hussain, R.; Smith, R. Synchrotron Radiation Circular Dichroism Spectroscopy Reveals That Gold and Silver Nanoparticles Modify the Secondary Structure of a Lung Surfactant Protein B Analogue. *Nanoscale* **2023**, *15* (9), 4591–4603. https://doi.org/10.1039/D2NR06107D.
(65) Kelly, S. M.; Jess, T. J.; Price, N. C. How to Study Proteins by Circular Dichroism. *Biochim. Biophys. Acta BBA - Proteins Proteomics* **2005**, *1751* (2), 119–139. https://doi.org/10.1016/j.bbapap.2005.06.005.
(66) Banerjee, R.; Sheet, T. Ratio of Ellipticities between 192 and 208 Nm (R_1): An Effective Electronic Circular Dichroism Parameter for Characterization of the Helical Components of Proteins and Peptides. *Proteins Struct. Funct. Bioinforma.* **2017**, *85* (11), 1975–1982. https://doi.org/10.1002/prot.25351.
(67) Olah, G. A.; Huang, H. W. Circular Dichroism of Oriented α Helices. I. Proof of the Exciton Theory. *J. Chem. Phys.* **1988**, *89* (4), 2531–2538. https://doi.org/10.1063/1.455047.
(68) Besley, N. A.; Hirst, J. D. Theoretical Studies toward Quantitative Protein Circular Dichroism Calculations. *J. Am. Chem. Soc.* **1999**, *121* (41), 9636–9644. https://doi.org/10.1021/ja990627l.
(69) Ramos, A. P. Dynamic Light Scattering Applied to Nanoparticle Characterization. In *Nanocharacterization Techniques*; Elsevier, 2017; pp 99–110. https://doi.org/10.1016/B978-0-323-49778-7.00004-7.
(70) Glatter, O. Dynamic Light Scattering (DLS). In *Scattering Methods and their Application in Colloid and Interface Science*; Elsevier, 2018; pp 223–263. https://doi.org/10.1016/B978-0-12-813580-8.00011-0.
(71) Sepúlveda, B.; Angelomé, P. C.; Lechuga, L. M.; Liz-Marzán, L. M. LSPR-Based Nanobiosensors. *Nano Today* **2009**, *4* (3), 244–251. https://doi.org/10.1016/j.nantod.2009.04.001.
(72) Mayer, K. M.; Hafner, J. H. Localized Surface Plasmon Resonance Sensors. *Chem. Rev.* **2011**, *111* (6), 3828–3857. https://doi.org/10.1021/cr100313v.
(73) Sui, M.; Kunwar, S.; Pandey, P.; Lee, J. Strongly Confined Localized Surface Plasmon Resonance (LSPR) Bands of Pt, AgPt, AgAuPt Nanoparticles. *Sci. Rep.* **2019**, *9* (1), 16582. https://doi.org/10.1038/s41598-019-53292-1.
(74) Petryayeva, E.; Krull, U. J. Localized Surface Plasmon Resonance: Nanostructures, Bioassays and Biosensing—A Review. *Anal. Chim. Acta* **2011**, *706* (1), 8–24. https://doi.org/10.1016/j.aca.2011.08.020.
(75) Ameer, F. S.; Varahagiri, S.; Benza, D. W.; Willett, D. R.; Wen, Y.; Wang, F.; Chumanov, G.; Anker, J. N. Tuning Localized Surface Plasmon Resonance Wavelengths of Silver Nanoparticles by Mechanical Deformation. *J. Phys. Chem. C* **2016**, *120* (37), 20886–20895. https://doi.org/10.1021/acs.jpcc.6b02169.

(76) Dennison, J. M.; Zupancic, J. M.; Lin, W.; Dwyer, J. H.; Murphy, C. J. Protein Adsorption to Charged Gold Nanospheres as a Function of Protein Deformability. *Langmuir* **2017**, *33* (31), 7751–7761. https://doi.org/10.1021/acs.langmuir.7b01909.
(77) Heller, C. Principles of DNA Separation with Capillary Electrophoresis. *ELECTROPHORESIS* **2001**, *22* (4), 629–643. https://doi.org/10.1002/1522-2683(200102)22:4<629::AID-ELPS629>3.0.CO;2-S.
(78) *Introduction to Capillary Electrophoresis*; Beckman Coulter.
(79) *Capillary Electrophoresis Methods for Pharmaceutical Analysis*, 1. ed.; Ahuja, S., Jimidar, M. I., Eds.; Separation science and technology; Elsevier/AP: Amsterdam, 2008.
(80) Yu, S.-B.; Zhou, P.; Feng, A.-R.; Shen, X.-C.; Zhang, Z.-L.; Hu, J.-M. PH Effect on Dynamic Coating for Capillary Electrophoresis of DNA. *Anal. Bioanal. Chem.* **2006**, *385* (4), 730–736. https://doi.org/10.1007/s00216-006-0407-4.
(81) Voeten, R. L. C.; Ventouri, I. K.; Haselberg, R.; Somsen, G. W. Capillary Electrophoresis: Trends and Recent Advances. *Anal. Chem.* **2018**, *90* (3), 1464–1481. https://doi.org/10.1021/acs.analchem.8b00015.
(82) Kanoatov, M.; Galievsky, V. A.; Krylova, S. M.; Cherney, L. T.; Jankowski, H. K.; Krylov, S. N. Using Nonequilibrium Capillary Electrophoresis of Equilibrium Mixtures (NECEEM) for Simultaneous Determination of Concentration and Equilibrium Constant. *Anal. Chem.* **2015**, *87* (5), 3099–3106. https://doi.org/10.1021/acs.analchem.5b00171.
(83) Krylov, S. N.; Berezovski, M. Non-Equilibrium Capillary Electrophoresis of Equilibrium Mixtures—Appreciation of Kinetics in Capillary Electrophoresis. *The Analyst* **2003**, *128* (6), 571–575. https://doi.org/10.1039/B212913B.
(84) Latreille, P.-L.; Le Goas, M.; Salimi, S.; Robert, J.; De Crescenzo, G.; Boffito, D. C.; Martinez, V. A.; Hildgen, P.; Banquy, X. Scratching the Surface of the Protein Corona: Challenging Measurements and Controversies. *ACS Nano* **2022**, *16* (2), 1689–1707. https://doi.org/10.1021/acsnano.1c05901.
(85) Boehmler, D. J.; O'Dell, Z. J.; Chung, C.; Riley, K. R. Bovine Serum Albumin Enhances Silver Nanoparticle Dissolution Kinetics in a Size- and Concentration-Dependent Manner. *Langmuir* **2020**, *36* (4), 1053–1061. https://doi.org/10.1021/acs.langmuir.9b03251.
(86) Wang, G.; Lu, Y.; Hou, H.; Liu, Y. Probing the Binding Behavior and Kinetics of Silver Nanoparticles with Bovine Serum Albumin. *RSC Adv.* **2017**, *7* (15), 9393–9401. https://doi.org/10.1039/C6RA26089F.
(87) Boehmler, D. J.; O'Dell, Z. J.; Chung, C.; Riley, K. R. Bovine Serum Albumin Enhances Silver Nanoparticle Dissolution Kinetics in a Size- and Concentration-Dependent Manner. *Langmuir* **2020**, *36* (4), 1053–1061. https://doi.org/10.1021/acs.langmuir.9b03251.
(88) Dasgupta, N.; Ranjan, S.; Patra, D.; Srivastava, P.; Kumar, A.; Ramalingam, C. Bovine Serum Albumin Interacts with Silver Nanoparticles with a "Side-on" or "End on" Conformation. *Chem. Biol. Interact.* **2016**, *253*, 100–111. https://doi.org/10.1016/j.cbi.2016.05.018.
(89) Lundqvist, M.; Sethson, I.; Jonsson, B.-H. Protein Adsorption onto Silica Nanoparticles: Conformational Changes Depend on the Particles' Curvature and the

Protein Stability. *Langmuir* **2004**, *20* (24), 10639–10647. https://doi.org/10.1021/la0484725.
(90) Hill, H. D.; Millstone, J. E.; Banholzer, M. J.; Mirkin, C. A. The Role Radius of Curvature Plays in Thiolated Oligonucleotide Loading on Gold Nanoparticles. *ACS Nano* **2009**, *3* (2), 418–424. https://doi.org/10.1021/nn800726e.
(91) Solveyra, E. G.; Szleifer, I. What Is the Role of Curvature on the Properties of Nanomaterials for Biomedical Applications? *Wiley Interdiscip. Rev. Nanomed. Nanobiotechnol.* **2016**, *8* (3), 334–354. https://doi.org/10.1002/wnan.1365.
(92) Afshinnia, K.; Gibson, I.; Merrifield, R.; Baalousha, M. The Concentration-Dependent Aggregation of Ag NPs Induced by Cystine. *Sci. Total Environ.* **2016**, *557–558*, 395–403. https://doi.org/10.1016/j.scitotenv.2016.02.212.
(93) Dennison, J. M.; Zupancic, J. M.; Lin, W.; Dwyer, J. H.; Murphy, C. J. Protein Adsorption to Charged Gold Nanospheres as a Function of Protein Deformability. *Langmuir* **2017**, *33* (31), 7751–7761. https://doi.org/10.1021/acs.langmuir.7b01909.
(94) Louche, A.; Salcedo, S. P.; Bigot, S. Protein–Protein Interactions: Pull-Down Assays. In *Bacterial Protein Secretion Systems*; Journet, L., Cascales, E., Eds.; Methods in Molecular Biology; Springer New York: New York, NY, 2017; Vol. 1615, pp 247–255. https://doi.org/10.1007/978-1-4939-7033-9_20.
(95) Yeo, E. L. L.; Azman, N. 'Ain; Kah, J. C. Y. Stealthiness and Hematocompatibility of Gold Nanoparticles with Pre-Formed Protein Corona. *Langmuir* **2021**, *37* (16), 4913–4923. https://doi.org/10.1021/acs.langmuir.1c00151.

Appendix

Table A1. Hydrodynamic diameter measurement values obtained by the DLS for single adsorbate systems.

Conditions		AgNPs only (nm)	AgNPs + BSA (nm)	AgNPs + SRHA (nm)
d_{AgNP} (nm)	10	76 ± 10	52 ± 1	59 ± 3
	20	39.2 ± 0.1	48 ± 20	46 ± 8
	40	52.0 ± 0.4	44 ± 2	49 ± 5

Table A2. PDI measurement values obtained by the DLS for single adsorbate systems.

Conditions		AgNPs only	AgNPs + BSA	AgNPs + SRHA
d_{AgNP} (nm)	10	0.3 ± 0.2	0.43 ± 0.02	0.38 ± 0.05
	20	0.4250 ± 6E-4	0.47 ± 0.04	0.44 ± 0.02
	40	0.260 ± 0.001	0.42 ± 0.09	0.40 ± 0.04

Table A3. Zeta potential measurement values obtained by the DLS for single adsorbate systems.

Conditions		AgNPs only (mV)	AgNPs + BSA (mV)	AgNPs + SRHA (mV)
d_{AgNP} (nm)	10	-40 ± 2	-37 ± 4	-37.1 ± 0.5
	20	-43 ± 1	-32 ± 1	-38.3 ± 0.4
	40	-42 ± 1	-32 ± 2	-39 ± 3

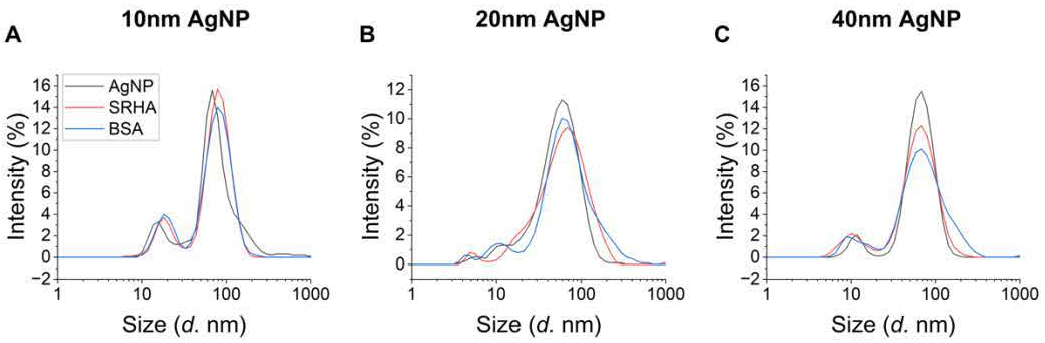

Figure A1. DLS size distributions for all single adsorbate conditions. Size distributions of pure AgNP (AgNP), AgNP with 60 mg L^{-1} SRHA (SRHA) and AgNP with 1 μM BSA (BSA) for **(A)** 10 nm, **(B)** 20 nm, and **(C)** 40 nm AgNP solutions. Samples were prepared in pre-concentrated (40 mg L^{-1}) AgNP solutions.

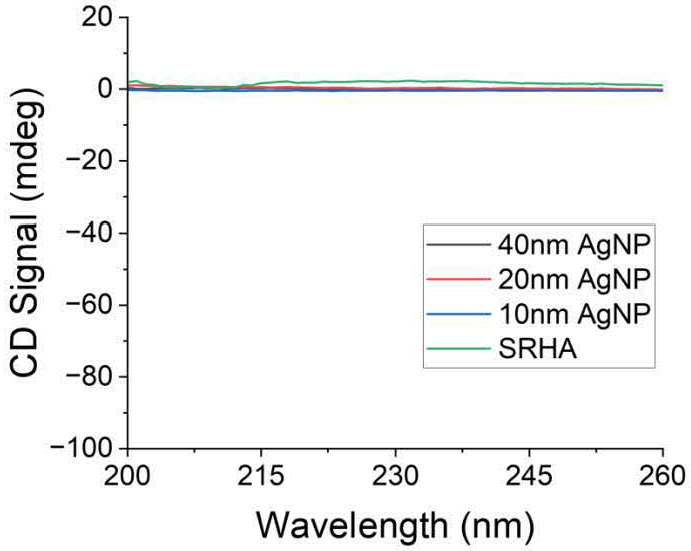

Figure A2. CD spectra of control samples only containing 60 mg L^{-1} SRHA in 10 mM sodium bicarbonate (pH 7.0) buffer (SRHA), and each of the pre-concentrated 10, 20, and 40 nm AgNPs (40 mg L^{-1}).

Table A4. CD α-helicity values calculated for all multi adsorbate conditions using equation 8.

Conditions		BSA only (%)	Comp (%)	Seq 1 (%)	Seq 2 (%)
d_{AgNP} (nm)	0	41.4 ± 0.3	24 ± 1	-	-
	10	41.3 ± 0.8	2 ± 3	0 ± 1	2 ± 3
	20	39 ± 1	2 ± 2	0 ± 1	0 ± 1
	40	40.9 ± 0.7	4 ± 1	2 ± 3	3 ± 5

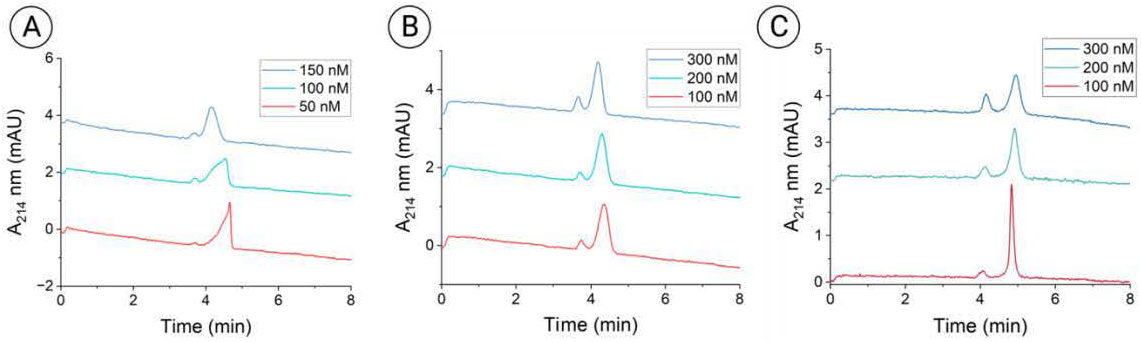

Figure A3. Representative NECEEM electropherograms. Representative NECEEM electropherograms of **(A)** 10 nm **(B)** 20 nm and **(C)** 40 nm AgNPs in solution with varying concentrations of BSA, as indicated, in solution.

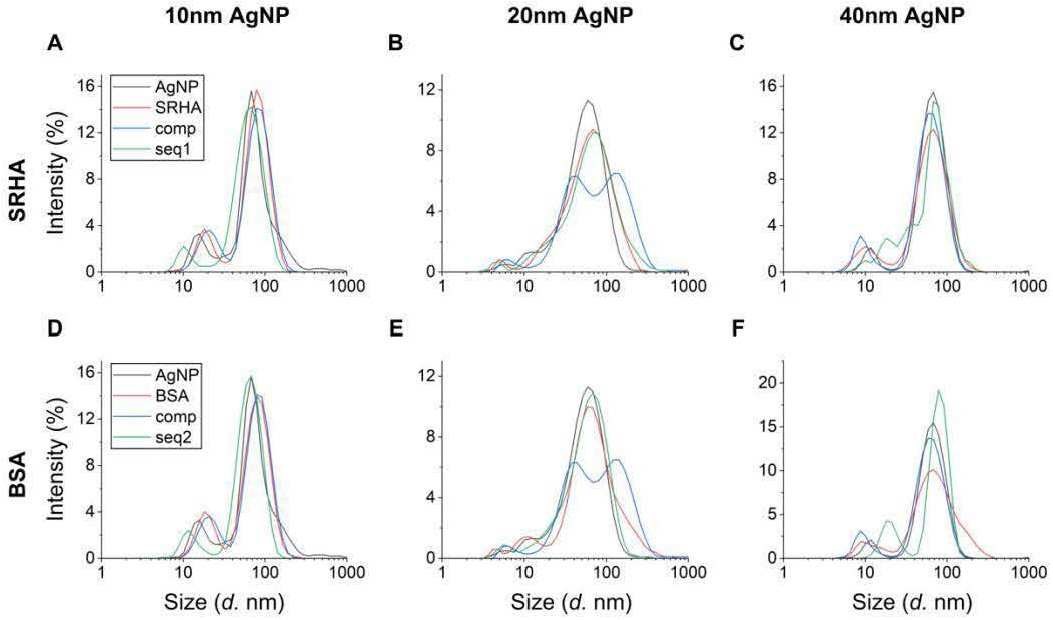

Figure A4. DLS size distributions for all multi adsorbate conditions. **(Top)** Effect of 60 mg L^{-1} SRHA on the diameter of **(A)** 10 nm **(B)** 20 nm **(C)** 40 nm AgNPs. **(Bottom)** Effect of 1 μM BSA on the diameter of **(D)** 10 nm **(E)** 20 nm **(F)** 40 nm AgNPs. AgNP denotes AgNPs prepared alone, (BSA and SRHA) denotes AgNPs prepared with either adsorbate, comp denotes AgNPs prepared simultaneously with SRHA and BSA, seq 1 denotes AgNPs sequentially incubated with BSA followed by SRHA, and seq 2 denotes AgNPs sequentially incubated with SRHA followed by BSA. All solutions contained 40 mg L^{-1} AgNPs in 10 mM sodium bicarbonate buffer solution (pH 7.0).

Table A5. Hydrodynamic diameter measurement values obtained by the DLS for multi adsorbate systems.

Conditions		AgNPs only (nm)	Comp (nm)	Seq 1 (nm)	Seq 2 (nm)
d_{AgNP} (nm)	10	76 ± 10	55 ± 3	49.1 ± 0.3	48.1 ± 0.1
	20	39.3 ± 0.1	52 ± 6	46 ± 10	41.1 ± 0.1
	40	52.9 ± 0.4	42.9 ± 0.7	150 ± 40	75 ± 16

Table A6. PDI measurement values obtained by the DLS for multi adsorbate systems.

Conditions		AgNPs only	Comp	Seq 1	Seq 2
d_{AgNP} (nm)	10	0.3 ± 0.2	0.42 ± 0.03	0.278 ± 0.003	0.279 ± 0.005
	20	0.4250 ± 6E-4	0.491 ± 0.005	0.47 ± 0.02	0.44 ± 0.01
	40	0.260 ± 0.001	0.43 ± 0.08	0.22 ± 0.03	0.27 ± 0.09

Table A7. Zeta potential measurement values obtained by the DLS for multi adsorbate systems.

Conditions		AgNPs only (mV)	Comp (mV)	Seq 1 (mV)	Seq 2 (mV)
d_{AgNP} (nm)	10	-41 ± 2	-34 ± 1	-33 ± 2	-38.8 ± 0.7
	20	-42.5 ± 0.8	-34 ± 2	-34.4 ± 0.8	-35 ± 1
	40	-42 ± 1	-39 ± 1	-34.8 ± 0.3	-35 ± 1

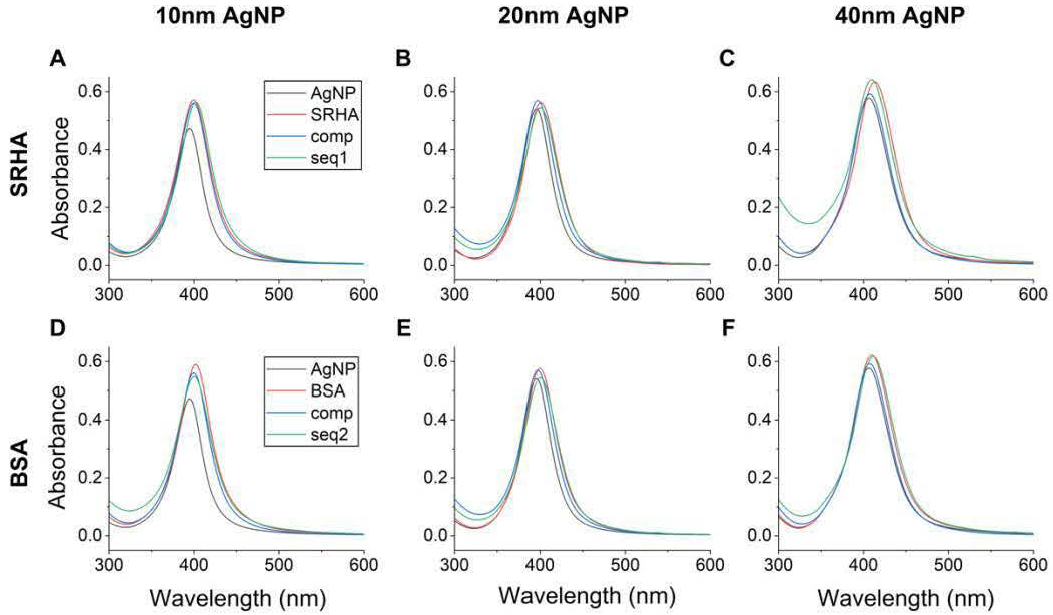

Figure A5. Full UV-Vis spectra runs spanning 300 to 600 nm for all multi adsorbate conditions. **(Top)** Effect of 60 mg L^{-1} SRHA on the diameter of **(A)** 10 nm **(B)** 20 nm **(C)** 40 nm AgNPs. **(Bottom)** Effect of 1 μM BSA on the diameter of **(D)** 10 nm **(E)** 20 nm **(F)** 40 nm AgNPs. AgNP denotes AgNPs prepared alone, (BSA and SRHA) denotes AgNPs prepared with either adsorbate, comp denotes AgNPs prepared simultaneously with SRHA and BSA, seq 1 denotes AgNPs sequentially incubated with BSA followed by SRHA, and seq 2 denotes AgNPs sequentially incubated with SRHA followed by BSA. All solutions contained 4 mg L^{-1} AgNPs in 10 mM sodium bicarbonate buffer solution (pH 7.0).

Table A8. % BSA_{bound} from pull-down assay and computed change in % BSA_{bound}.

Conditions		BSA only (%)	BSA + SRHA (%)	Δ % BSA_{bound} (%)
d_{AgNP} (nm)	10	44 ± 3	37 ± 3	15.0
	20	8 ± 3	2 ± 1	70.5
	40	1.1 ± 0.8	0.7 ± 0.5	40.0